PE&RS

May 2024

Volume 90, Number 5

PHOTOGRAMMETRIC ENGINEERING & REMOTE SENSING

The official journal for imaging and geospatial information science and technology asprs THE IMAGING & GEOSPATIAL INFORMATION SOCIETY

ASPRS MEMBERSHIP

WHERE DO YOU WANT TO GO? WHOM DO YOU WANT TO BECOME?

Joining ASPRS is a great way to boost your resume and learn valuable life lessons

WHY GET INVOLVED WITH ASPRS?

- Develop leadership skills
- Experience working on a team
- Gain valuable soft skills
- Network
- Learn about yourself
- Have fun!

Scholarships

The many ASPRS scholarships are only available to student members

Certification

The ASPRS certification program for mapping scientists, photogrammetrists and technologists is the only fully Accredited certification program in the geospatial sciences

Continuing Education

Earn professional development hours and CEUs by attending workshops at our conferences and on-line as well as our monthly on-line geobytes series

PE&RS

Our monthly journal, is packed with informative and timely articles designed to keep you abreast of current developments in your field. Now available in e-format.

Get Connected

facebook.com/ASPRS.org

linkedin.com/company/asprs/about/

twitter.com/ASPRSorg

YouTube youtube.com/user/ASPRS

Image and text courtesy the ASPRS Florida Region

asprs FLORIDA REGION THE IMAGING & GEOSPATIAL INFORMATION SOCIETY

To have your press release published in *PE&RS*, contact Rae Kelley, rkelley@asprs.org.

ANNOUNCEMENTS

As of April 4, 2024, **Surdex**, surdex.com, has officially joined Bowman. Bowman is a leading national professional services firm offering multi-disciplinary engineering, planning, surveying, geomatics, construction management, environmental consulting, landscape architecture, and right-of-way acquisition. This change provides a strong foundation for our firms to merge our comprehensive skillsets while offering the same level of commitment to deliver outstanding project results, build long-lasting relationships and leverage the growth of our organization to serve the ever-changing needs of our clients.

"The acquisition of Surdex will align well with our strategic objectives of expanding our geospatial service offerings, growing our public sector market presence, and increasing the average size of our acquisitions," said Gary Bowman, chairman and CEO of Bowman. "Surdex's portfolio of high-resolution image capture, orthoimage processing, and digital mapping services provides tremendous revenue synergy opportunities with our customers. Adding state-of-the-art, high-altitude services to Bowman's extensive array of terrestrial and low-altitude capabilities will create a compelling suite of full-service geospatial solutions. From the outset, the Surdex operation will realize savings by utilizing Bowman's current survey resources and Bowman will experience cost savings by accessing Surdex's high-volume image processing resources. We believe this acquisition will be transformational for our geospatial business and look forward to quickly integrating our teams and capabilities."

"Bowman's size and access to the broader engineering services market is what attracted us to this transaction," said Ron Hoffmann, president of Surdex. "We have been a family business for almost 70 years and because of that, we were very selective about who we would entrust with this transition. Over the past several months, we have become extremely confident in our conclusion that partnering with Bowman is the right decision for our business, our employees, and our customers."

Industry leaders in the architecture, engineering, and construction (AEC) sectors are increasingly relying on the interoperability of geographic information systems (GIS) and building information modeling (BIM) to reduce costs and boost efficiency across construction projects. In support of AEC organizations, **Esri**, www.esri.com, and Autodesk, are expanding their strategic alliance.

"Esri is proud to bring this new integration to Autodesk users, empowering them with enhanced visibility of existing conditions for better-informed design decisions that reduce environmental impacts," said Kathleen Kewley, Esri director for AEC global business development.

The integration of ArcGIS Basemaps with Civil 3D and AutoCAD provides AEC professionals with detailed geospatial data and mapping capabilities. The new integrations further unify GIS and BIM, delivering real business value to architects, engineers, planners, and contractors.

"Unleashing the power of ArcGIS Basemaps in Civil 3D and AutoCAD provides users with an unparalleled geographical perspective, driving precision in decision-making and fostering a more sustainable built environment," said Eric DesRoche, Autodesk senior manager, infrastructure strategy, AEC design. "This new integration is a testament to our unwavering commitment to innovation and collaboration."

"ArcGIS Basemaps serves as the cornerstone of our mapping products," said Bridget Brown, Geospatial and Information Management Director for HDR, a user of Esri and Autodesk software. "These carefully styled basemaps not only offer vital location context but also liberate our teams from creating them from the ground up, allowing us to concentrate on project-specific data. Additionally, the capability to customize these basemaps using the vector tile style editor empowers us to unlock new realms of cartographic creativity when needed."

"ArcGIS Basemaps are the contextual canvas that establishes one of the most important elements when answering the question of 'where'," said Darin Welch, Associate Vice President, Design, Geospatial, and Community Intelligence, HNTB Digital Transformation Solutions, another Esri and Autodesk user. "Esri's basemaps have equipped our teams with immediate and accurate representation of the surrounding world, and the situational awareness necessary for making the best transportation decisions for improving our communities."

NV5 Global, Inc., www.nv5.com, has reached an agreement to acquire GIS Solutions, Inc. ("GIS Solutions"), a full range provider of enterprise geographic information system (GIS) technologies and services including GIS application development, cloud-based database design, data science, and project management. GIS Solutions supports state departments of transportation and utilities by developing solutions that monitor asset management, expedite efficient service delivery, and deliver real time mapping and incident reporting. The acquisition was made with a combination of cash and stock and will be immediately accretive to NV5's earnings.

"Tech-enabled services, such as geospatial solutions, have grown as a percentage of NV5's revenue as we focus on services with higher margins and more rapid scalability than traditional surveying services, and we are pleased to add GIS Solutions to the NV5 organization," said Dickerson Wright, PE, Executive Chairman of NV5. "We will continue to identify and pursue opportunities in geospatial and other tech-enabled service categories to drive margin expansion and organic growth throughout NV5."

GIS Solutions specializes in developing web-enabled GIS database applications from multiple modalities to track and monitor transportation resources and asset conditions for departments of transportation, a growing sector in the geospatial market. GIS Solutions also provides cloud-managed and systems design services to help organizations employ geospatial solutions. Applications may be utilized in cloud-based environments, networked desktop solutions, and mobile applications to meet the unique accessibility and security requirements of clients and their constituents.

"We are excited to join the NV5 team, and we look forward to the growth opportunities available to our valued employees as part of the nation's largest geospatial data analytics firm," said Jim Conlon, President of GIS Solutions.

GPI Geospatial, Inc., www.gpinet.com, (a subsidiary of Greenman-Pedersen, Inc.) has been a leading geospatial solutions company for over 50 years with a footprint across the Eastern U.S., and they recently upgraded their mobile mapping capabilities by adding a RIEGL VMX-2HA to their data collection portfolio. As a RIEGL, www.rieglusa.com, customer for several years in various market verticals, GPI has enhanced their mobile offerings by upgrading their previous VMX-450 to the VMX-2HA. This top-of-the-line RIEGL mobile mapping system will keep them at the forefront of technology and allow them to provide the most precise and efficient deliverables to their clients all while increasing "in the field" productivity.

"GPI Geospatial will use this advanced new mobile LiDAR and spherical camera system to support multiple initiatives, including our roadway and DOT clients, GIS Asset Inventory projects, pavement condition inspection tasks, and railway projects." said Paul Badr, President of GPI Geospatial. "This new system will enhance our collection efforts by maximizing safety and efficiency in both the field and the office, allowing us to serve our clients better."

GPI Geospatial has had a long successful history of mobile mapping collection projects." said Joshua France, RIEGL USA's Mobile Division Manager. "Over the years, the team got a lot of miles out of their VMX-450 systems, and the RIEGL VMX-2HA will only expand their mobile mapping abilities. We are excited to be a trusted partner of GPI Geospatial and look forward to many more successful projects including rail and highway mapping."

GPI Geospatial has had a long successful history of mobile mapping collection projects." said Joshua France, RIEGL USA's Mobile Division Manager. "Over the years, the team got a lot of miles out of their VMX-450 systems, and the RIEGL VMX-2HA will only expand their mobile mapping abilities. We are excited to be a trusted partner of GPI Geospatial and look forward to many more successful projects including rail and highway mapping."

As the GPI mobile acquisition team hits the road with their brand new VMX system, their dedication to innovation and client satisfaction aligns with RIEGL's commitment to developing and producing unparalleled cutting edge LiDAR technology with unwavering customer support. RIEGL USA looks forward to further collaboration and successful future project highlights.

Vexcel Data Program, https://vexceldata.com/, announced it will expand its global coverage of high-resolution aerial imagery by adding new countries to its planned collection for 2024: Brazil, South Africa, Estonia, Latvia, Lithuania, and Poland. With this expansion, Vexcel is set to become the only aerial imagery collection program operating on every continent, except Antarctica.

"This expansion further solidifies Vexcel's position as the world's largest aerial imagery program," shared Erik Jorgensen, CEO of Vexcel Group. "Our focus is to continue to provide the type of aerial data that's required to support the visualization and analysis needs of today's customers in more places than ever before. And we continue to grow our footprint globally to serve the needs of our customers with imagery that delivers on quality and accuracy."

Vexcel will collect high-resolution aerial imagery in urban areas across the new countries, delivering highly detailed information to improve decision-making, support better remote assessment, create digital twins, and monitor assets with ease. Customers can improve their location intelligence with multiple points of view, such as north, south, east, west views of Oblique imagery, and top-down views of TrueOrtho. This imagery will be published at 7.5cm resolution.

In addition, Digital Surface Model (DSM) data will also be available as well as Vexcel's AI-derived Elements product line which uses its high-resolution imagery to deliver automated attributes on buildings, properties, and transportation assets.

Vexcel's urban country collection program offers imagery at a native resolution multiple times better than satellite imagery and with significantly better geographic positional accuracy. It's delivering the highest caliber of aerial imagery for better location intelligence to solve real-world problems with greater ease. Its robust library of imagery and geospatial data in 40+ countries and territories help a variety of industries, such as Government, Telecom, Utilities, Insurance, AEC, Energy, Technology, HD Mapping, and more.

The imagery will become available in the Vexcel Platform, APIs, Image Services for ArcGIS, and through partner platforms, as it is released throughout 2024.

CALENDAR

- 13-16 May, **Geospatial World Forum**, Rotterdam, The Netherlands; https://geospatialworldforum.org.
- 20-22 May, **STRATUS 2024**, Syracuse, New York; https://stratus-conference.com/home/.
- 3-7 June, **URISA GIS Leadership Academy**, Seattle, Washington; https://urisa.org/page/URISA_AdvancedGLA.
- 11-14 June, **ISPRS Technical Commission II Symposium — The Role of Photogrammetry for a Sustainable World**, Las Vegas, Nevada; www.isprs.org/tc2-symposium2024.
- 15-19 July, **Esri User Conference**, San Diego, California; www.esri.com/en-us/about/events/uc/overview.
- 18-22 August, **SPIE 2024**, San Diego, California; https://spie.org/OP.
- 7-10 October, **GIS-Pro 2024**, Portland, Maine; https://urisa.org/page/GIS-Pro2024.

PE&RS

PHOTOGRAMMETRIC ENGINEERING & REMOTE SENSING

The official journal for imaging and geospatial information science and technology

May 2024 Volume 90 Number 5

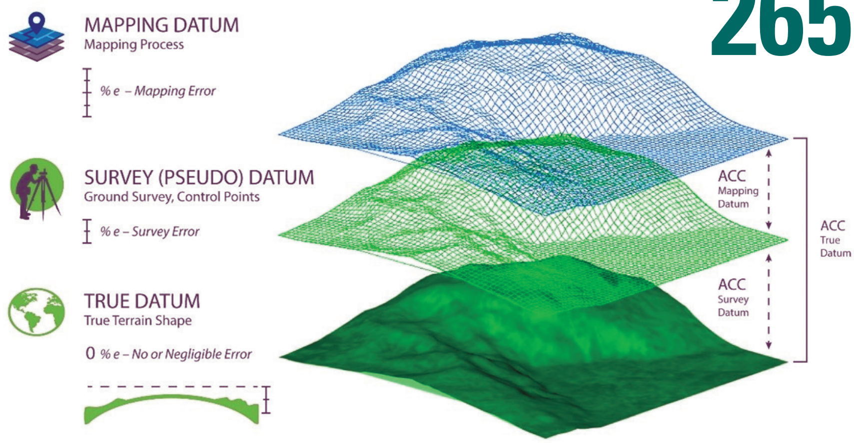

COLUMNS

ANNOUNCEMENTS

DEPARTMENTS

See the Cover Description on Page 264

COVER DESCRIPTION

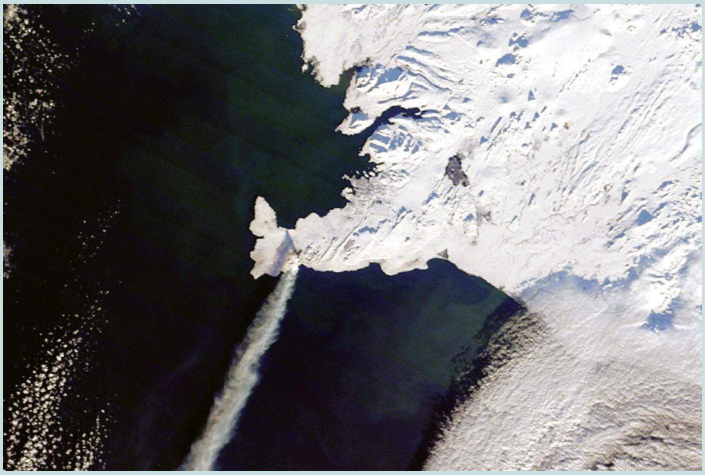

After a lull in activity, fresh lava has once again poured from the Reykjanes peninsula in southwestern Iceland.

The latest eruption—the third in the region since December 2023—began early on February 8, 2024, with lava spraying up to heights of 80 meters (260 feet) along a 3-kilometer (1.8-mile) long fissure near Mount Sýlingarfell. The small peak is north of the fishing village Grindavík and east of the Svartsengi power station and Blue Lagoon geothermal spa.

The cover image was acquired on February 10, 2024, by the OLI-2 (Operational Land Imager-2) on Landsat 9. Infrared and visible observations (bands 7-6-3) have been overlain on a natural-color image to help distinguish the heat signature of the lava. Still recent but cooler lava expelled near Grindavík in January appears black.

The topography around the fissure meant that much of the fresh lava flowed east into unpopulated areas rather than south toward Grindavík. Some lava also flowed west into the vicinity of the power plant and spa.

Earthen defensive walls protected both facilities, though lava did burn through a key hot water pipeline and two roads. According to the Icelandic National Broadcasting Service RÚV, authorities are in the process of restoring hot water to homes in the area after conducting repairs on the pipeline.

About seven hours after the eruption began, the MODIS (Moderate Resolution Imaging Spectroradiometer) on NASA's Terra satellite captured this image of a plume of gas and ash streaming to the southwest. This eruption was effusive—not explosive like the Eyjafjallajökull eruption in 2010—and the plume contained minimal ash, so it did not cause any disruptions to either domestic or international flights.

Volcanic plumes like the one shown here typically contain water vapor, sulfur dioxide, carbon dioxide, and small amounts of other volcanic gases. Researchers from the Icelandic Met Office and the University of Iceland have noted that, at times, magma has interacted with groundwater, adding to the amount of water vapor in the plume. The TROPOMI (Tropospheric Monitoring Instrument) on the Sentinel-5 Precursor mission observed sulfur dioxide (SO2) within the plume, Michigan Tech volcanologist Simon Carn noted on X.

After the initial burst of activity on February 8, the intensity of the eruption faded. In an update on February 9, the Icelandic Met Office reported that seismic sensors had stopped detecting volcanic tremors and that a recent drone flight showed no activity over the eruption site—signs that the latest eruption was ending.

However, on February 12, the agency reported that the land surface above an underground magma reservoir near Svartsengi had again begun to swell by 0.5 to 1 centimeters per day, a rate similar to what was observed prior to other recent eruptions. "It is therefore highly likely that the cycle continues in a few weeks with another dyke propagation and a volcanic eruption," the agency said.

NASA Earth Observatory image by Lauren Dauphin, using MODIS data from NASA EOSDIS LANCE and GIBS/Worldview. Story by Adam Voiland.

Both images can be viewed online by visiting the Landsat Image Gallery, https://landsat.gsfc.nasa.gov/, image id 152428.

PHOTOGRAMMETRIC ENGINEERING & REMOTE SENSING

Journal Staff

Publisher ASPRS
Editor-In-Chief Alper Yilmaz
Director of Publications Rae Kelley
Electronic Publications Manager/Graphic Artist Matthew Austin

Photogrammetric Engineering & Remote Sensing is the official journal of the American Society for Photogrammetry and Remote Sensing. It is devoted to the exchange of ideas and information about the applications of photogrammetry, remote sensing, and geographic information systems. The technical activities of the Society are conducted through the following Technical Divisions: Geographic Information Systems, Photogrammetric Applications, Lidar, Primary Data Acquisition, Professional Practice, Remote Sensing Applications, and Unmanned Autonomous Systems. Additional information on the functioning of the Technical Divisions and the Society can be found in the Yearbook issue of *PE&RS*.

All written correspondence should be directed to the American Society for Photogrammetry and Remote Sensing, PO Box 14713, Baton Rouge, LA 70898, including general inquiries, memberships, subscriptions, business and editorial matters, changes in address, manuscripts for publication, advertising, back issues, and publications. The telephone number of the Society Headquarters is 225-408-4747; the fax number is 225-408-4422; web address is www.asprs.org.

PE&RS. *PE&RS* (ISSN0099-1112) is published monthly by the American Society for Photogrammetry and Remote Sensing, 8550 United Plaza Blvd, Suite 1001, Baton Rouge, Louisiana 70809 . Periodicals postage paid at Bethesda, Maryland and at additional mailing offices.

SUBSCRIPTION. *PE&RS* is available as an e-Subscription (single-site and multi-site licenses) and an e-Subscription with print add-on (single-site license only). PE&RS subscriptions are on a calendar-year, beginning in January and ending in December.

The rate for a single-site e-Subscription for the USA/Non-USA is $1040 USD, for Canadian* is $1092 USD.

The rate for a multi-site e-Subscription for the USA/Non-USA is $1040 USD plus $250 USD for each additional license, for Canadian* is $1092 USD plus $263 for each additional license.

The rate for e-Subscription with print add-on for the USA is $1546 USD, for Canadian* is $1637 USD, and for Non-USA is $1596 USD.

*Note: Subscription prices for Canada includes 5% of the total amount for Canada's Goods and Services Tax (GST #135123065). **PLEASE NOTE: All Subscription Agencies receive a 20.00 USD discount.**

POSTMASTER. Send address changes to PE&RS, ASPRS, PO Box 14713, Baton Rouge, LA 70898. CDN CPM #(40020812).

MEMBERSHIP. Membership is open to any person actively engaged in the practice of photogrammetry, photointerpretation, remote sensing and geographic information systems; or who by means of education or profession is interested in the application or development of these arts and sciences. Membership is for one year, with renewal based on the anniversary date of the month joined. Membership Dues include a 12-month electronic subscription to *PE&RS*. Annual Individual Membership dues are $175.00 USD and Student Membership dues are $50.00 USD. A tax of 5% for Canada's Goods and Service Tax (GST #135123065) is applied to all members residing in Canada.

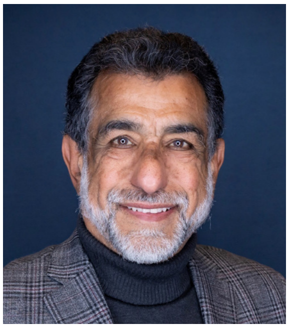

Best Practices in Evaluating Geospatial Mapping Accuracy according to the New ASPRS Accuracy Standards

By Qassim Abdullah, Ph.D., PLS, CP, Woolpert Vice President and Chief Scientist

This highlight article was inspired by a comment I received from Mr. Richard C. Maher, PLS, President of KDM Meridian, where he said:

> "I attended *both of your American Society for Photogrammetry and Remote Sensing (ASPRS) workshops during Geo Week 2024 in Denver. Even after 24 years as a land surveyor, I can still use refreshing on how to explain the basics to my clients and to surveyors-in-training. Your in-depth discussion on the difference between the Standard Deviation (SD) and the Root-Mean-Squares (RMSE) was very appreciated. I also appreciated the concepts of the true datum and the survey (pseudo) datum you introduced. As one who loves to test and prove that our equipment can rarely do better than the specifications, I'll say unequivocally that surveyors using Real-Time Kinematic (RTK) positioning are far too optimistic about their true accuracy and commonly don't understand apparent relative accuracy due to a fundamental misunderstanding of the error sources different between GPS and conventional measurements. The nature of random error in GPS follows a different stochastic model than conventional instrumentation. If surveyors simply employed the same checking standards and methods you prescribe in the ASPRS Specifications, they'd stop telling me how well their GPS did under a canopy, or how they can get "hundredths". My intention isn't to make their work more difficult but to ensure that our methods are rigorous and reliable... I'm interested in seeing your future appendix that talks about suggested survey accuracies when not provided by surveyors. Due to the importance of these topics to the thousands of practicing surveyors in the nation who could not attend Geo Week, could you please shed light on the concepts you presented in Denver regarding surveying and mapping accuracy and the role of the correct understanding of the datum play in it?"*

In my response to Mr. Maher's request, I will address these important issues in separate sections, easier for the reader to follow and digest.

Standard Deviation Versus Root-Mean-Squares Errors Estimation

Before we discuss the difference between the two statistical measures of Standard Deviation and the RMSE as accuracy measures, let us elaborate on the statistical meaning of each of them.

Standard Deviation

Standard Deviation is a statistical measure for the fluctuation or dispersion of individual errors around the mean value of all errors in dataset. Figure 1 illustrates how the errors fluctuate around a mean error value of 0.17m. Such fluctuation is represented by the standard deviation value, or 0.07m.

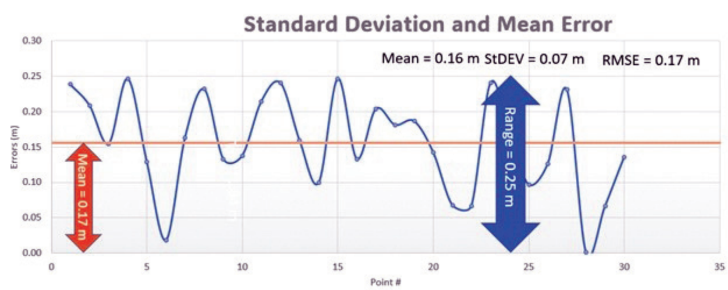

Figure 1. Standard deviation measures the error fluctuation around a mean value of 0.17m.

The Standard Deviation is calculated as the square root of variance by determining each error's deviation relative to the mean as given in the following equation:

$$s_x = \sqrt{\frac{1}{(n-1)}\sum_{i=1}^{n}(x_i - \overline{x})^2}$$

where:

$\overline{x}$ is the mean error in the specified direction,

x_i is the i^{th} error in the specified direction,

n is the number of checkpoints tested,

i is an integer ranging from 1 to n.

Photogrammetric Engineering & Remote Sensing
Vol. 90, No. 5, May 2024, pp. 265-272.
0099-1112/22/265-272

doi: 10.14358/PERS.90.5.265

Root-Mean-Square Error (RMSE)

RMSE is the square root of the average of the set of squared differences between data set coordinate values and coordinate values from an independent source of higher accuracy for identical points. It is obvious from such definition that RMSE differs from Standard Deviation by the magnitude of the error mean existing in the data. That becomes clear when you analyze the last equation of the standard deviation and the following Root-Mean-Square Error:

$$RMSE_x = \sqrt{\frac{1}{n}\sum_{i=1}^{n}(x_{i(map)} - x_{i(surveyed)})^2}$$

where:

$x_{i(map)}$ is the coordinate in the specified direction of the i^{th} checkpoint in the data set,

$x_{i(surveyed)}$ is the coordinate in the specified direction of the i^{th} checkpoint in the independent source of higher accuracy,

n is the number of checkpoints tested,

i is an integer ranging from 1 to n.

When RMSE is computed, we do not subtract the mean error from the checkpoint error, so RMSE represents the full spectrum of the error that found in a checkpoint including the mean error, while in computing the standard deviation, we subtract the mean error from every checkpoint error making it a measure for the fluctuation of individual errors around the mean value of all errors. This RMSE characteristic makes it useful in flagging biases in data, as it provides an early warning system for the technician that the standard deviation fails to do so.

Biases and Systematic Errors in Data

Now, we understand the difference between the standard deviation and RMSE, let us see how such favoring of the RMSE helps the Geospatial mapping production process and validating the accuracy of its products. Geospatial mapping products are subject to systematic errors or biases from a variety of sources. These biases can be caused by things like using the wrong version of a datum during the product production process, or using the wrong instrument height for the tripod during the survey computations for the ground control points or the checkpoints. There are other sources of biases that can be introduced during the production processes. For instance, using the wrong elevation values in a digital elevation data can results in biases during the orthorectification process, and using the wrong camera parameters (such as focal length) or the wrong lens distortion model can lead to biases in the final mapping product.

Systematic error can cause the product to fall below acceptable project accuracy levels. Thankfully, provided the appropriate methodologies are applied, systematic error can be identified, modeled, and removed from the data. This is not the case with random error: even if we discover it, we cannot eliminate it. However, we can minimize random error magnitude through adherence to stringent production process, adopting sound quality control practices, or the use of more accurate instruments. To illustrate systematic errors or biases in data, we will evaluate the scoreboards of four archers that vary in their aiming skills, illustrated in Figure 2.

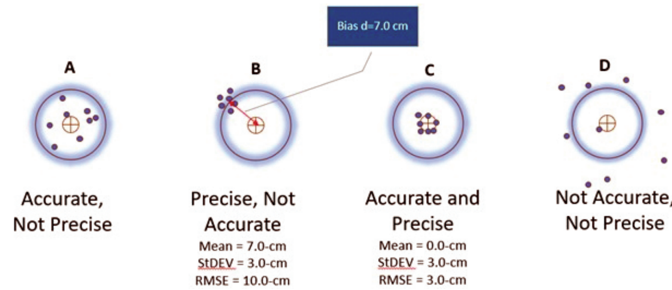

Figure 2. Scoreboards for four archers with varied aiming skills.

For board A, the archer landed the arrows around the bullseye, but the shots are scattered spatially around the center point. By contrast, board B reflects good spatial clustering, but the shots are clustered around a point far away from the bullseye. Board C is what you want your accuracy to be, with all shots clustered at the spot aimed for. Board D demonstrates extremely undesirable results, possessing neither good clustering, nor good aiming.

When we measure accuracy, results like boards B and C are the most desirable. Board C should be preferred, as it represents clean results: all shots are at the bullseye. We can describe Archer C as "accurate and precise". Although Archer B's results lack good aim, the shots are clustered well; here we describe Archer B as "precise but not accurate". Even though Archer B is not accurate, why are these results still acceptable? Examine the scoreboard for Archer B again: if we shift the locations of all the clustered arrows by a fixed distance d, or 7.0-cm, the results will match the results from board C. This distance d or 7.0-cm represents the systematic error; once it is corrected, the final accuracy will be satisfactory.

But why did such a precise archer miss the bullseye to begin with? We must consider what may have taken place at the archery range to cause Archer B to miss. Perhaps the archer was using a sight scope hooked to the archer bow. Having all the arrows land in a tight cluster away from the bullseye is a strong indication of a mechanical failure of the sight scope that caused the arrows to go to the wrong place. Once Archer B's sight scope is properly calibrated, the archer scoreboard in the second archery session will look just like Archer C's board. The same logic can be applied to geospatial products like lidar point clouds or orthoimagery. That is why it is crucial to use accurate checkpoints when verifying product accuracy. Such checkpoints will help us quantify any existing systematic errors, allowing us to remove this error from the data in the same way that properly calibrating Archer B's sight scope corrected the archer future shots.

True Daum Versus Surveying Psudo Datum

When we conduct field surveying, we are trying to determine terrain positions and shapes in reference to a specific geodetic datum. According to the U.S. National Geodetic Survey (NGS), a geodetic datum is defined as "an abstract coordinate system with a reference surface (such as sea level, as a vertical datum) that serves to provide known locations to begin surveys and create maps." Because our surveying techniques, and therefore our mapping techniques, are not perfect, our surveying techniques only provide approximate positions that put us close to the true, datum-derived positions (Figure 3). When we use an inaccurately surveyed network to control another process such as aerial triangulation, in reality we are fitting the aerial triangulation solution to an observed datum. The degree of approximation depends on the accuracy of the surveying technique or technology employed in that survey. The RTK field surveying technique, for example, can produce positions that are accurate to 2cm horizontally and perhaps 2-3cm vertically. The differential leveling technique used to determine height can produce elevations that are accurate to the sub-centimeter. The lesson to learn here is that our surveying techniques, no matter how accurate, do not represent the true datum—but they can get us close to it.

Surveying and Survey (Pseudo) Datum

When we task surveyors to survey the ground control network in reference to a certain datum, usually a true datum such as NAD83 or WGS84, they can only determine the positions of the control network to that datum as close as the surveying techniques allow. In other words, the coordinates that are being used to control the mapping process represent an observed or survey datum that represents a pseudo datum, green mesh in Figure 3, but not the original intended or true datum represented with the solid green in Figure 3. For example, if we are trying to determine point coordinates in NAD83(2011), the surveyed coordinates used in aerial triangulation or lidar calibration represent a datum that is close to NAD83(2011) but not exactly NAD83(2011) due to the inaccuracy in our surveying techniques. That inaccurate survey represents a survey datum. Besides the inaccuracy in the surveying techniques, another layer of errors (i.e., distortion) could be added to the surveyed coordinates when we convert geographic positions (in latitude and longitude) to projected coordinates or grid coordinates, such as state plane coordinate systems.

Mapping to the Mapping Datum

Any mapping process we conduct today inherits two modeling errors that influence product accuracy. The first modeling error is caused by the inaccuracy of the internal geometric determination during the aerial triangulation, or the boresight calibration in the case of lidar processing. The second modeling error is introduced by the auxiliary systems, such as GPS and IMU, and has inherent errors caused by the survey datum. Therefore, when we use mapping products to extract location information, we are determining these locations in reference to the survey or pseudo datum and not the true intended datum. The point coordinates for NAD83(2011) are determined not according to the survey datum of the ground control network but through a new reality of mapping datum. The mapping datum, represented with the blue mesh in Figure 3, inherits the errors of the survey datum, which were caused by the inaccuracy of our surveying techniques and the errors caused by our mapping processes and techniques $ACC_{SurveyDatum}$ and $ACC_{MappingDatum}$ in Figure 3.

Correct Approach to Accuracy Computation

To reference the accuracy of determining a mapped object location within a mapping product to the original intended datum like NAD83(2011), we need to examine the layers of errors that were introduced during the ground surveying and mapping processes (Figure 3).

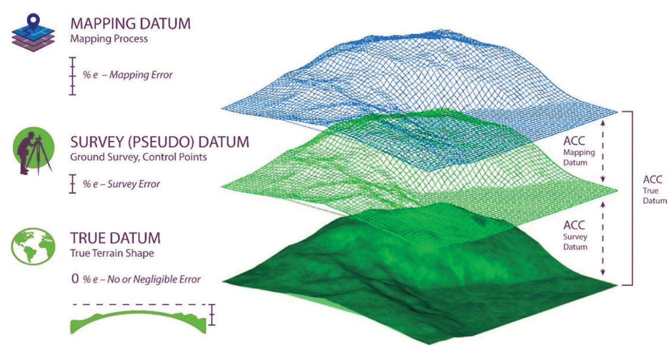

Figure 3. Datums and error propagation in geospatial data.

Currently, users of geospatial data express product accuracy based on the agreement or disagreement of the tested product per the surveyed checkpoints, ignoring checkpoint or ground control errors that have resulted from inaccurate surveying techniques. In other words, users consider the surveyed points to be free of error. The following section details how errors are propagated into the mapping product when we are trying to determine the location of a ground point "A". Let us introduce the following terms, refer to Figure 3 for localizing such error terms:

$ACC_{SurveyDatum}$ equals the accuracy in determining the survey datum, generated when realizing the intended or true datum through surveying techniques. In other words, it represents the errors in the surveyed checkpoints. Due to this inaccuracy, the point will be located at location A¨ (Figure 4).

$ACC_{MappingDatum}$ equals the accuracy of determining the mapping datum, or the errors introduced during the mapping process, in reference to the already inaccurate survey datum represented by the surveyed checkpoints. In other words, it is the fit of the aerial triangulation (for imagery) or the boresight/calibration (for lidar) to the surveyed ground control points represented as the survey datum. This accuracy is measured using the surveyed checkpoints during the product accuracy verification process. Due to this inaccuracy, the point will be located at location A$^{\cdots}$ (Figure 4).

$ACC_{TrueDatum}$ equals the accuracy of the mapping product in reference to the true datum, as in NAD83(2011). The point location A$^{\cdot}$ (Figure 4) is considered the most accurate location determined in reference to the true datum.

Using the above definitions, the correct product accuracy should be modeled using error propagation principles according to the following formula:

$$ACC_{TrueDatum} = \sqrt{ACCMappingDatum^2 + ACCSurveyDatum^2} \;...\; (1)$$

However, according to our current practices, product accuracy is computed according to the following formula, ignoring errors in the surveying techniques:

$$ACC_{TrueDatum} = ACC_{MappingDatum} \;......................................\; (2)$$

More details and examples on the suggested approach can be found in my published article[1] on the topic and Edition 2, V2 of the ASPRS Positional Accuracy Standards for Digital Geospatial Data.

The New Approach in Computing Map Accuracy

According to this new approach on computing maps accuracy and since we are dealing with three-dimensional error components, we would need to employ vector algebra to accurately compute the cumulative error.

Computing Horizontal Accuracy

To compute the horizontal accuracy for a two-dimensional map, as with orthorectified imagery, we will ignore the error component of the height survey. In other words, we will use the error component from easting and northing only. We will also assume that the accuracy of determining the X coordinates (or easting) is equal to the accuracy of determining the Y coordinates (or northing). Using error propagation principles and Euclidean vector in Figures 4 and 5, we can derive the following values for product horizontal accuracy:

$$AccXTrueDatum = \sqrt{AccXTrueDatum^2 + AccXSurveyDatum^2} \;....\; (3)$$

$$AccYTrueDatum = \sqrt{AccXTrueDatum^2 + AccYSurveyDatum^2} \;...\; (4)$$

$$AccXYTrueDatum = \sqrt{AccXTrueDatum^2 + AccYTrueDatum^2} \;.....\; (5)$$

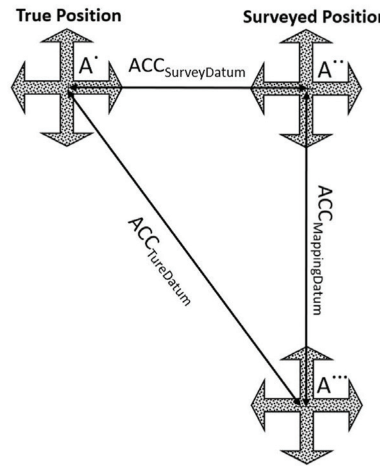

Figure 4. Influence of error propagation on point location accuracy

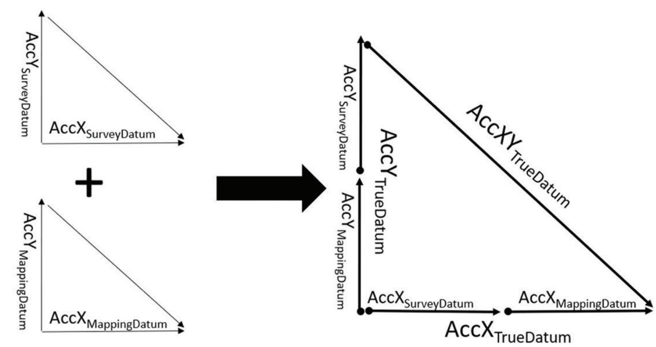

Figure 5. Vector representations of error components.

As an example, when modeling horizontal product accuracy according to the above formulas, let us assume the following:

a) We are evaluating the horizontal accuracy for orthoimagery using independent checkpoints.
b) The control survey report states that the survey for the checkpoints, which was conducted using RTK techniques, resulted in accuracy of $RMSE_{XorY}$ equal to 2cm.
c) When the checkpoints were used to verify the horizontal accuracy of the orthoimagery, it resulted in an accuracy of $RMSE_{XorY}$ equal to 3cm.

"ASPRS positional accuracy standard advise that a mean error value that is more than 25% of the RMSE, is an indication of biases in the data that need to be dealt with and resolved before accepting and delivering the Lidar data."

[1] Abdullah, Q., Rethinking Error Estimations in Geospatial Data: The Correct Way to Determine Product Accuracy, *Photogrammetric Engineering & Remote Sensing*, Vol. 86, No. 7, July 2020, pp. 397–403.

Solution
Using equations 3, 4 and 5:

$$AccXTrueDatum = \sqrt{AccXMappingDatum^2 + AccXSurveyDatum^2} = \sqrt{3^2 + 2^2} = 3.61cm$$

$$AccYTrueDatum = \sqrt{AccYMappingDatum^2 + AccYSurveyDatum^2} = \sqrt{3^2 + 2^2} = 3.61cm$$

$$AccXYTrueDatum = \sqrt{AccXTrueDatum^2 + AccYTrueDatum^2} = \sqrt{3.61cm^2 + 3.61cm^2} = 5.1cm$$

The value of 5.1cm is the true accuracy of the product versus the following value of 4.24cm used commonly today that ignores the errors introduced during the ground surveying process:

$$AccXYTrueDatum = \sqrt{AccXMappingDatum^2 + AccYMappingDatum^2} = \sqrt{3cm^2 + 3cm^2} = 4.24cm$$

Computing Vertical Accuracy

Similarly, for vertical accuracy determination of elevation data derived from lidar or photogrammetric methods, we need to consider the error in the surveyed elevation as an important component. Using error propagation principles and Euclidean vector of Figure 6, we can derive the following value for vertical product accuracy:

$$AccZTrueDatum = \sqrt{AccZMappingDatum^2 + AccZSurveyDatum^2} \ldots(6)$$

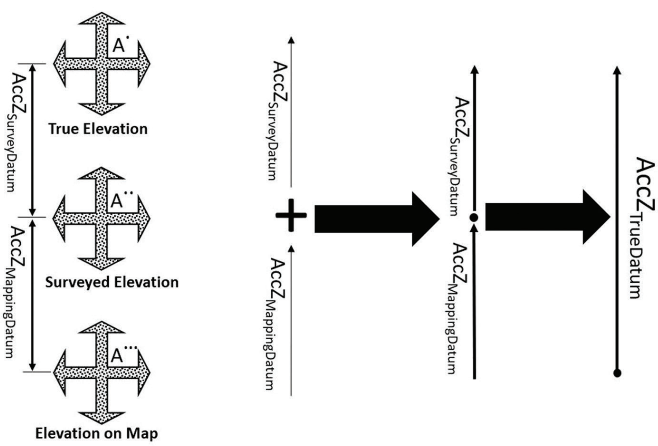

Figure 6. Influence of error propagation on point elevation accuracy.

As an example, when modeling vertical product accuracy according to the above formulas, let us assume the following:

a) That we are evaluating the vertical accuracy for a mobile lidar dataset using independent checkpoints.
b) The control survey report states that the survey of the checkpoints, which was conducted using RTK techniques, resulted in an accuracy of $RMSE_Z$ equal to 3cm
c) When the checkpoints were used to verify the vertical accuracy of the lidar data, it resulted in an accuracy of $RMSE_Z$ equal to 1cm.

Solution
Using Equation 6:

$$AccZTrueDatum = \sqrt{AccZMappingDatum^2 + AccZSurveyDatum^2} = \sqrt{1^2 + 3^2} = 3.16cm$$

The value of 3.16cm is the true vertical accuracy of the lidar dataset versus the value of 1cm, derived by the mapping technique used commonly that ignores the errors introduced during the ground surveying process.

The Role of RMSE in Revealing Biases in Data

Now, let's see how we are going to assess the accuracy computations, and whether we can spot problems in the data. We now assume a scenario in which systematic error was introduced into a lidar dataset during the product generation. Say a technician used the wrong version of the geoid model when converting the ellipsoidal heights of the point cloud to orthometric heights, which caused a systematic error or bias of 0.16 m in the computed elevation of the processed lidar point cloud. Table 1 lists the results of the accuracy assessment where 30 check points used for the test.

To analyze the accuracy results, first, look at the error mean value in table 1. We clearly notice that the mean error is high as compared to the RMSE and the standard deviation. ASPRS positional accuracy standard advise that a mean error value that is more than 25% of the RMSE, is an indication of biases in the data that need to be dealt with and resolved before accepting and delivering the Lidar data. So, we will focus on the results in Table 1 for further analysis. A high mean error value is a good indication that biases are present in the data, but we need to further investigate how high the mean value is compared to RMSE and standard deviation. Slight differences between these statistical measures' values are acceptable. Looking at the results of Table 1, the mean error reaches 91% of the RMSE value which is not acceptable by the ASPRS positional accuracy standard measures. We also need to compare the RMSE to the standard deviation. Note that they are 0.069 m and 0.170 m, respectively. Having an RMSE value that is more than twice the standard deviation is a strong indication that biases may be present in the data. Remember, in the absence of systematic error, i.e., biases, the RMSE and the standard deviation should be equal. This conclusion is also supported by the fact that the mean is twice as high as the standard deviation.

Now that we have concluded that the data has biases in it, let us see how we will remove this bias without reproducing the product from scratch. For lidar data, we will need to raise or lower the computed heights for the point cloud by the amount of the bias—in this case, 0.16 m. Since the mean is a positive value, and the values in the "Error Values" column were computed by subtracting the lidar elevation from the checkpoint elevation, or:

Error = Surveyed Elevation – Lidar Elevation

we can then conclude that the terrain elevation as determined from the lidar data is lower than that measured by the surveyed checkpoints. Thus, we need to raise the lidar elevation by 0.16 m. Table 2 illustrates the bias treatment we introduced above where the modified accuracy assessment values are listed in column "Unbiased Error Values". All we did here was raising, or z-bump, the elevations of the point cloud by the amount of the bias, 0.16 m.

Similarly, if such analysis were conducted to investigate the horizontal positional accuracy of an orthoimage, all we would need to do is modify the coordinates of the tile's header by the amount of the calculated biases without the need to reproduce the orthoimages. It is worth mentioning that removing the bias based on the "mean" value will not necessarily reduce the value of the RMSE by the same amount, as the degree of improvement in the recalculated RMSE value depends on the value of the standard deviation. For data sets with low standard deviation value and low rates of fluctuation, removal of the biases will improve the RMSE by a more significant degree. With the data cleaned from the bias effect, all conditions for good accuracy results are satisfied and clearly presented in Table 2. The mean error is zero as it was removed, and the standard deviation and the RMSE values are equal.

Table 1. Accuracy assessment for a biased dataset.

Point #	Surveyed Coordinates			Lidar	Error Values (m)
	Easting (m)	Northing (m)	Elevation (m)	Elevation (m)	
CP_1	746093.605	97840.580	332.708	332.469	0.239
CP_2	746084.481	97875.486	333.856	333.646	0.209
CP_3	746076.993	97906.423	334.791	334.636	0.155
CP_4	746069.043	97934.869	335.829	335.582	0.247
CP_5	746059.191	97968.525	336.837	336.708	0.129
CP_6	746051.284	97996.814	337.671	337.652	0.018
CP_7	746044.837	98025.039	338.717	338.553	0.163
CP_8	746036.494	98055.805	339.823	339.591	0.232
CP_9	746027.369	98082.550	340.646	340.513	0.134
CP_10	746019.781	98112.192	341.636	341.498	0.138
CP_11	746012.222	98144.373	342.792	342.577	0.215
CP_12	746006.094	98171.008	343.667	343.426	0.241
CP_13	745998.080	98196.380	344.486	344.326	0.160
CP_14	745987.766	98231.319	345.597	345.498	0.100
CP_15	745939.681	98221.349	347.036	346.789	0.247
CP_16	745950.670	98190.848	345.788	345.655	0.133
CP_17	745956.968	98166.660	344.999	344.795	0.204
CP_18	745966.818	98133.845	343.825	343.644	0.182
CP_19	745977.417	98100.689	342.676	342.489	0.187
CP_20	745986.146	98071.263	341.594	341.451	0.143
CP_21	745994.431	98044.637	340.573	340.505	0.068
CP_22	746003.437	98011.200	339.403	339.336	0.067
CP_23	746013.675	97977.662	338.426	338.185	0.241
CP_24	746020.633	97952.708	337.451	337.282	0.169
CP_25	746029.450	97922.620	336.316	336.219	0.097
CP_26	746037.820	97896.313	335.422	335.295	0.127
CP_27	746073.182	98205.333	343.418	343.186	0.231
CP_28	746137.202	98304.228	344.254	344.253	0.001
CP_29	746046.203	97866.550	334.320	334.253	0.067
CP_30	746056.297	97832.573	333.199	333.063	0.136
		Number of Checkpoints			30
		Minimum Error			0.001
		Maximum Error			0.247
		Mean Error			0.156
		Median Error			0.157
		Standard Deviation			0.069
		RMSE			0.170
		Horizontal Positional Accuracy (E & N)			N/A
		Vertical Positional Accuracy			0.170
		3D Positional Accuracy			N/A

Table 2. Accuracy assessment after bias removal.

Point #	Surveyed Coordinates			Biased Lidar	Unbiased Lidar	Unbiased Error Values (m)
	Easting (m)	Northing (m)	Elevation (m)	Elevation (m)	Elevation (m)	
CP_1	746093.605	97840.580	332.708	332.469	332.625	0.083
CP_2	746084.481	97875.486	333.856	333.646	333.802	0.053
CP_3	746076.993	97906.423	334.791	334.636	334.792	-0.001
CP_4	746069.043	97934.869	335.829	335.582	335.738	0.091
CP_5	746059.191	97968.525	336.837	336.708	336.864	-0.027
CP_6	746051.284	97996.814	337.671	337.652	337.808	-0.138
CP_7	746044.837	98025.039	338.717	338.553	338.709	0.007
CP_8	746036.494	98055.805	339.823	339.591	339.747	0.076
CP_9	746027.369	98082.550	340.646	340.513	340.669	-0.022
CP_10	746019.781	98112.192	341.636	341.498	341.654	-0.018
CP_11	746012.222	98144.373	342.792	342.577	342.733	0.059
CP_12	746006.094	98171.008	343.667	343.426	343.582	0.085
CP_13	745998.080	98196.380	344.486	344.326	344.482	0.004
CP_14	745987.766	98231.319	345.597	345.498	345.654	-0.056
CP_15	745939.681	98221.349	347.036	346.789	346.945	0.091
CP_16	745950.670	98190.848	345.788	345.655	345.811	-0.023
CP_17	745956.968	98166.660	344.999	344.795	344.951	0.048
CP_18	745966.818	98133.845	343.825	343.644	343.800	0.026
CP_19	745977.417	98100.689	342.676	342.489	342.645	0.031
CP_20	745986.146	98071.263	341.594	341.451	341.607	-0.013
CP_21	745994.431	98044.637	340.573	340.505	340.661	-0.088
CP_22	746003.437	98011.200	339.403	339.336	339.492	-0.089
CP_23	746013.675	97977.662	338.426	338.185	338.341	0.085
CP_24	746020.633	97952.708	337.451	337.282	337.438	0.013
CP_25	746029.450	97922.620	336.316	336.219	336.375	-0.059
CP_26	746037.820	97896.313	335.422	335.295	335.451	-0.029
CP_27	746073.182	98205.333	343.418	343.186	343.342	0.075
CP_28	746137.202	98304.228	344.254	344.253	344.409	-0.155
CP_29	746046.203	97866.550	334.320	334.253	334.409	-0.089
CP_30	746056.297	97832.573	333.199	333.063	333.219	-0.020
			Number of Checkpoints			30
			Minimum Error			-0.155
			Maximum Error			0.091
			Mean Error			0.000
			Median Error			0.001
			Standard Deviation			0.069
			RMSE			0.067
			Horizontal Positional Accuracy (E & N)			N/A
			Vertical Positional Accuracy			0.067
			3D Positional Accuracy			N/A

The New Approach and Challenges for Users

As we introduced the new approach in modeling products accuracy, I was surprised by the following findings:

Survey Accuracy and Surveyors Awareness

As expressed in equation 1, the new approach requires the user to enter an absolute accuracy figure for the surveyed local network. To my surprise, I found many surveyors I spoke with, were either not aware of where to find such accuracy figure in the instrument processing report, or they blindly trust some numbers that reported in such reports, where the accuracy is presented as quality measure that does not relate to the absolute accuracy that the new approach calls for. I reviewed several processing reports from some surveying instruments where such figure approaches zero., i.e. 0.002 m.

Table 3. Best Predicted Accuracies for Surveying Techniques[1].

Survey Methodology	Best Predicted Accuracy Values		
	Horizontal	Vertical	3D
Adjusted Closed Loop – Digital Levelling		5mm	
Real Time Network Following Section C – Recommended Procedures	10mm	16mm	19mm
Real Time PPP After Convergence Following Section D – Recommended Procedures	15mm	24mm	28mm
Rea Time Kinematic (RTK) Single Measurement Following Section B – Recommended Procedures	20mm	32mm	38mm
Closed Conventional Traverse Following Section E – Recommended Procedures	25mm	40mm	47mm
Real Time PPP After Convergence, Single Measurement	20mm	50mm	54mm

[2] Addendum II of the ASPRS Positional Accuracy Standards, Edition 2, V2.

Surveying Instruments Manufacturers and Survey Accuracy

To that affect, the ASPRS accuracy standard working group contacted several manufacturers of surveying instruments, but we did not get a straight answer to our request as most manufacturers do not report such absolute accuracy figures. To me, it seems such a reported accuracy figure of close to zero, represents a precision measure from multiple survey sessions of the same point. Users of such instruments need to know that all current surveying instruments, no matter how accurate, cannot produce a surveying accuracy of 0.002 meter.

Surveyors and Mappers Power

Surveyors and other users of such instruments need to unite their efforts to exert some efforts with the surveying equipment manufacturers to provide access to the absolute accuracy of the network survey, without it we cannot comply with the accuracy assessment method dictated by the new ASPRS positional accuracy standard. For the time being, and until manufacturers provide us with such accuracy, Table 3 that we included in the forthcoming version of the ASPRS Positional Accuracy Standards can be used as the default accuracy values in situations where the survey accuracy is not available or known.

"Surveyors and other users of such instruments need to unite their efforts to exert some efforts with the surveying equipment manufacturers to provide access to the absolute accuracy of the network survey"

The Need to Revise the Professional Practice Certifcation Programs

The issues raised in this article are a clear indication of the lack of awareness among professionals about the very issue impacting basic surveying and mapping practices. I call on all professional societies such as NSPS, ASPRS, ASCE, TRB, and others to lead an awareness campaign to educate their members on the importance of this issue. The time is right to start such a campaign as we head towards an entire National Spatial Reference System (NSRS) modernization program that the NOAA and the NGS are leading us to. The new North American Terrestrial Reference Frame of 2022 (NATRF2022) and the North American-Pacific Geopotential Datum of 2022 (NAPGD2022) will offer more accurate and evolving horizontal and vertical datum which makes the issues raised in this article even more crucial to the success of our business. Similarly, I put forward a call to all state agencies which are tasked with the professional certification of surveyors, mappers, and engineers and the NCEES to revise their certification testing materials to include topics raised in this article. Without doing this, we risk the health, safety, and welfare of the public.

This article will be published concurrently in Lidar Magazine.

GIS Tips & Tricks

By Al Karlin, Ph.D., CSM-L, GISP

Need More Tools? Try These...

Geoprocessing tools are the nuts of bolts of GIS processing. An "off-the-shelf" GIS software package could come with several hundred standard tools. But what are the options for a beginning or intermediate GIS analyst when you face a GIS question that requires a new or different tool. Well… there are actually multiple options available, some easier to access than others. Below are a few "tips" for finding tools not included with the off-the-shelf GIS products. Please note that these are options, and not endorsements or recommendations.

For ArcGIS (Desktop and Pro)

Tip #1 — Although off-the-shelf ArcGIS Pro comes with 41 toolboxes, there is always room for one more. One of my favorite "add-ins" is Arc Hydro (Figure 1). If you are looking for tools directed specifically for water resources, this is the toolset for you. This toolbox is available from Esri, at no cost, https://www.esri.com/en-us/industries/water-resources/arc-hydro/downloads?rsource=https%3A%2F%2Fdownloads.esri.com%2Farchydro%2Farchydro%2FSetup%2F.

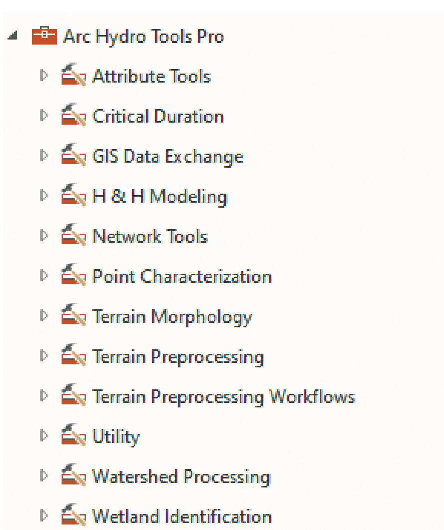

Figure 1. The Esri Arc Hydro Toolset in ArcGIS Pro.

This toolset is available for most versions of ArcGIS Desktop (ArcMap 9.3 and higher), as well as, ArcGIS Pro (2.5 and higher) and comes with a wealth of documentation. Best of all, just download the .MSI file, double-click on it and it installs itself. The "gottcha" with this toolset is that Esri is constantly upgrading it with new tools and functionality. The version number will be in the "Settings | Apps | Installed apps" description if you forgot to note it somewhere, so after a few months, you might want to update. (Hint: I generally append the version number to the downloaded .MSI file along with the date I downloaded it.)

Tip #2 — For those a little more adventurous and willing to accept an "AS IS" add-in, the WhiteBox tools (Figure 2) from MIT are a really good choice. This Python-based toolset brings a wide variety of GIS functions, some of which overlap with the "off-the-shelf" tools, but there are several unique tools; Machine Learning and Precision Agriculture for example.

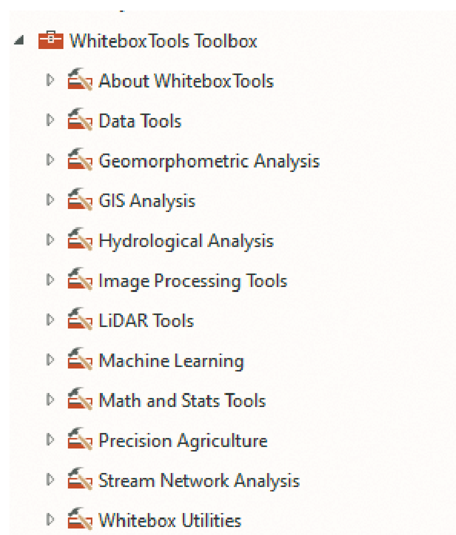

Figure 2. The WhiteBox Toolset in ArcGIS Pro.

The WhiteBox toolset for ArcGIS is available at no cost from GitHub, https://github.com/opengeos/WhiteboxTools-ArcGIS/tree/master/WBT . The WhiteBox tools are also available as a Python, Jupyter, and R library. Installation is pretty easy and the toolset is available "adding" the toolset to the Toolboxes in ArcGIS Pro | Catalog.

Photogrammetric Engineering & Remote Sensing
Vol. 90, No. 5, May 2024, pp. 273-274.
0099-1112/22/273-274

doi: 10.14358/PERS.90.5.273

Tip 3 — For those less adventurous and more financially solvent, there are several commercially available add-in toolsets. One of the more robust while still economical packages is a tried-and- true package called "XTools". This toolset is offered as a "try before you buy" package that includes more than 100 tools and functions for spatial analysis, shape conversions and table management. There are versions available for both ArcGIS Desktop and ArcGIS Pro that can be downloaded from https://xtools.pro/en/overview/.

For QGIS

Tip #4 — The Whitebox toolset is also available to QGIS users. There is a Python Plugin Repository, https://plugins.qgis.org/plugins/wbt_for_qgis/ .

Tip #5 — QGIS maintains a large repository of plug-ins that cover a wide range of GIS analytics, ranging from Shape and Lat/Long Tools to Rubbersheeting and Image Classification. These and more are available at no cost for download at: https://plugins.qgis.org/.

For "Free" GIS Software

Tip #6 — While the above tips assume that you are using either an Esri product or an opensource product, like QGIS, there are other "free" downloadable options, and some even run on MacOS, a rarity in the GIS world. It may take a bit of patience to find the right product for your analysis, but GISGeography.com (https://gisgeography.com/free-gis-software/) is a good place to start your search.

Finally, while you are at the GISGeography.com site, for the most adventurous, there are several Python libraries (https://gisgeography.com/python-libraries-gis-mapping/) tutorials, and other support documentation to "make your own" tools.

Send your questions, comments, and tips to GISTT@ASPRS.org.

Al Karlin, Ph.D., CMS-L, GISP is with Dewberry's Geospatial and Technology Services group in Tampa, FL. As a senior geospatial scientist, Al works with all aspects of lidar, remote sensing, photogrammetry, and GIS-related projects.

SAVE THE DATE!

2024 ASPRS INTERNATIONAL TECHNICAL SYMPOSIUM

October 21-25, 2024

For more information, visit
https://my.asprs.org/2024symposium

NEW ASPRS MEMBERS

ASPRS would like to welcome the following new members!

Devon Borthwick
Bradley Peter Bowyer
Kristopher Brandt
Eric Lee Cole
Thomas Dempsey
Samantha Doss-Watson
Jeremy Foote
Benjamin Ghansah
Michael Hoppus
Adam Bruce Hutson
Shannon Grace Meade
Michael Glenn Murphy
Gavin Norman
Francisco Ortimio Rangel
Christopher Daniel Rose
Gerardo Arturo Sanchez-Azofeifa, PhD
Tim Stiles
Monte Turner, PhD
Ruilin Wang
Sage Michelle Wright

FOR MORE INFORMATION ON ASPRS MEMBERSHIP, VISIT
HTTP://WWW.ASPRS.ORG/JOIN-NOW

WHO'S WHO IN ASPRS

Founded in 1934, the American Society for Photogrammetry and Remote Sensing (ASPRS) is a scientific association serving thousands of professional members around the world. Our mission is to advance knowledge and improve understanding of mapping sciences to promote the responsible applications of photogrammetry, remote sensing, geographic information systems (GIS) and supporting technologies.

BOARD OF DIRECTORS

BOARD OFFICERS

President
Bandana Kar
U. S. Department of Energy (DOE)

President-Elect
Amr Abd-Elrahman
University of Florida

Vice President
Alvan Karlin, PhD, CMS-L, GISP
Dewberry

Past President
Lorraine B. Amenda, PLS, CP
Towill, Inc

Treasurer
John McCombs
NOAA

Secretary
Harold Rempel
ESP Associates, Inc.

COUNCIL OFFICERS

ASPRS has six councils. To learn more, visit https://www.asprs.org/Councils.html.

Sustaining Members Council
Chair: Paul Badr
Deputy Chair: Melissa Martin

Technical Division Directors Council
Chair: Hope Morgan
Deputy Chair: Tao Liu

Early-Career Professionals Council
Chair: Greg Stamnes

Region Officers Council
Chair: Demetrio Zourarakis
Deputy Chair: Cody Condron

Committee Chairs Council
Chair: David Day

Student Advisory Council
Chair: Oscar Duran
Deputy Chair: Ali Alruzuq

TECHNICAL DIVISION OFFICERS

ASPRS has seven professional divisions. To learn more, visit https://www.asprs.org/Divisions.html.

Geographic Information Systems Division
Director: Jin Lee
Assistant Director: Michael Baranowski

Lidar Division
Director: Matt Bethel
Assistant Director: Nora May

Photogrammetric Applications Division
Director: Hank Theiss
Assistant Director: Jae Sung Kim

Primary Data Acquisition Division
Director: Srini Dharmapuri
Assistant Director: Ravi Soneja

Professional Practice Division
Director: Hope Morgan
Assistant Director: Christian Stallings

Remote Sensing Applications Division
Director: Tao Liu
Assistant Director: Indu Jeyachandran

Unmanned Autonomous Systems (UAS)
Director: Bahram Salehi
Assistant Director: Rebecca Capps

REGION PRESIDENTS

ASPRS has 13 regions to serve the United States. To learn more, visit https://www.asprs.org/regions.html.

Alaska Region
Dave Parret

Cascadia Region
Jimmy Schulz

Eastern Great Lakes Region
Craig Fry

Florida Region
Matt LaLuzerne

Gulf South
Cody Condron

Heartland Region
Whit Lynn

Mid-South Region
David Hughes

North Atlantic Region
Kurt Lutz

Northeast Region
Trevis Gigliotti

Pacific Southwest Region
Omar Mora

Potomac Region
Jason Brown

Rocky Mountain Region
Trent Casi

Western Great Lakes Region
Adam Smith

A Pixel Texture Index Algorithm and Its Application

Xiaodan Sun and Xiaofang Sun

Abstract

Image segmentation is essential for object-oriented analysis, and classification is a critical parameter influencing analysis accuracy. However, image classification and segmentation based on spectral features are easily perturbed by the high-frequency information of a high spatial resolution remotely sensed (HSRRS) image, degrading its classification and segmentation quality. This article first presents a pixel texture index (PTI) by describing the texture and edge in a local area surrounding a pixel. Indeed.. The experimental results highlight that the HSRRS image classification and segmentation quality can be effectively improved by combining it with the PTI image. Indeed, the overall accuracy improved from 7% to 14%, and the kappa can be increased from 11% to 24%, respectively. Five supervised evaluative indicators (i.e., oversegmentation, undersegmentation, edge-matching degree, number of segmentation blocks, and shape error) have reduced from 27.6% to 75%.

Introduction

In recent years, high spatial resolution remotely sensed (HSRRS) images with multi-spectral bands such as WorldView-II, IKONOS, and QuickBird (Blaschke *et al.* 2014) have provided copious amounts of data for many fields, such as marine, forestry, agricultural resource management, dynamic land use monitoring, disaster prevention, and assessment, population census, and mineral resource development and utilization. Accordingly, the development and improvement of image analysis technology promote the application potential of HSRRS images, which is also a crucial aspect of remote sensing technology.

Object-oriented analysis is generally used for HSRRS images, as an object provides more features than pixel-oriented analysis, making HSRRS image analysis more intelligent, accurate, and efficient (Blaschke *et al.* 2014; Chen *et al.* 2017). The HSRRS image has sharp high-frequency information, e.g., texture and edges. However, the spectral values within the same land-cover type are more complex, reducing the HSRRS image's classification and segmentation quality. Segmentation is essential for object-oriented analysis, and classification is key in influencing analysis accuracy (Corcoran *et al.* 2010; Lin *et al.* 2019). To overcome this problem, we simultaneously combined the texture features and edges of land-cover types during classification and segmentation, effectively reducing the misclassification caused by the spectral homogeneity of the different land-cover types and the "oversegmentation" phenomenon caused by the spectral heterogeneity of the same land-cover type. Therefore, simultaneously obtaining the texture features and edges of various land-cover types prior to image segmentation or classification is a problem to be solved.

The texture is essential to identifying land-cover types and is generated by the regular changes in the image's spectral features. Currently, the following texture-based methods have been proposed: (1) Statistical analysis description methods that obtain first-order, second-order, or higher-order statistical texture features of an object, which include the gray-level co-occurrence matrix (GLCM) (Palm 2004; Samiappan *et al.* 2017; Zhang *et al.* 2020), semi-variance graph (Balaguer *et al.* 2010; He and Changqing 2011; Wu *et al.* 2015), and autocorrelation function (Lin *et al.* 1997; Brochard *et al.* 2001; Hu *et al.* 2018). This description method is simple and easy to use and implement. Its texture analysis process differs significantly from the human visual mechanism and is sensitive to image noise. (2) Geometric structure description methods that extract an object's texture primitives (i.e., the basic texture elements) and copy and arrange them according to preset rules to characterize the texture features, such as syntactic texture analysis (Lu and Fu 1978; Arvor *et al.* 2013) and mathematical morphology (Decenciere *et al.* 2001; Feng *et al.* 2021). This method is only appropriate for describing regular textures, as its ability to describe irregular textures is inadequate. (3) Extraction of texture features by using time-frequency and multi-scale signal processing analysis techniques (e.g., wavelet, Gabor, Fourier, and discrete cosine transforms) (Arivazhagan and Ganesan 2003; Arivazhagan *et al.* 2006; Zhang *et al.* 2006; Qian *et al.* 2012; Rebhi *et al.* 2019; Teillet *et al.* 2021;Zhang and Li. 2022). Texture features are classified as high-frequency information and can be easily decomposed into noise during signal processing. (4) Model description methods (e.g., Markov random field, fractal model, and autoregression model) (Alata and Olivier 2003; Dai *et al.* 2020; Padhy *et al.* 2021) that use model parameters to represent texture features. Since model training is an iterative optimization process, these methods have high time–space complexity. (5) Graph theory description methods that use graph theory (e.g., local graph structure and tourist walking map) (Backes *et al.* 2010; Sayeed *et al.* 2013; Abdullah *et al.* 2014; Liu *et al.* 2015) to analyze the texture and extract some significant graphical data (e.g., points, lines, and planes) to describe the texture features. Typically, this method is used for facial recognition and textile identification. (6) The machine learning description method, which is based on a large amount of training sample data in the texture library, obtains texture feature description data through machine/deep learning (such as extreme learning machine and convolutional neural network) (Andrearczyk and Whelan 2016; Duan *et al.* 2017; Liu and Ren. 2022; Zhang *et al.* 2022). This method requires collecting a large amount of texture sample data, and the calculation process is complex, time-consuming, and labor-intensive. (7) Entropy-based methods, such as the two-dimensional sample entropy method, the two-dimensional distribution entropy method, and the two-dimensional multi-scale entropy method, that analyze the correlation between the irregularity and complexity of the texture from the perspective of two-dimensional space and extract the entropy measurement data to characterize the texture features (Zunino and Ribeiro 2016; Silva *et al.* 2018; Espinosa *et al.* 2021). This type of method is better suited to describe irregular and complex textures.

However, existing methods can only extract texture features, most of which are used for image classification or object identification, while no method can simultaneously extract an object's texture and edge features for image classification or segmentation. So far, pixel-level indices (such as Normalized Difference Vegetation Index, NDVI and Normalized Difference Water Index, NDWI) have highlighted

Xiaodan Sun is with the College of Fuzhou Polytechnic and the Fujian Artificial Intelligence Collaborative Innovation Center (xsun@fvti.edu.cn). Xiaodan Sun is also with the College of Fuzhou Polytechnic and the Fujian Artificial Intelligence Collaborative Innovation Center (xsun@fvti.edu.cn).

Xiaofang Sun is with the College of Geography and Oceanography, Minjiang University.

Corresponding author: Xiaodan Sun (xsun@fvti.edu.cn)

Contributed by Desheng Liu, June 23, 2023 (sent for review December 2, 2023; reviewed by Caiyun Zhang, Jason A. Tullis, Xiaoyu Liang).

Photogrammetric Engineering & Remote Sensing
Vol. 90, No. 5, May 2024, pp. 277–292.
0099-1112/22/277–292

doi: 10.14358/PERS.23-00051R2

the thematic information in images from the perspective of spectral features. NDVI is a remote sensing index used for measuring vegetation coverage and growth conditions, while NDWI is a remote sensing index used for detecting water bodies and wetlands. Nevertheless, no one has proposed a pixel-level index highlighting various texture and edge features of land features. Based on the current situation, this article proposes an algorithm to analyze ground texture and edge features from the perspective of pixels. Specifically, the developed algorithm obtains pixel texture index (PTI) image data by evaluating the contextual relationship of texture features between pixels in a local area. In PTI images, the homogeneity of texture and edge features of various ground features can be reflected. Combining PTI image data can effectively improve the classification and segmentation quality of HSRRS images.

The rest of this article is organized as follows. “Principles and Methods” describes the PTI algorithm. “Experiments” discusses the application of the PTI algorithm in the classification and segmentation of HSRRS images such as QuickBird and WorldView-II. “Results and Analysis” analyzes and evaluates the experimental results. Finally, the article ends with “Conclusions.”

Principles and Methods

In order to briefly discuss the principles and methods proposed in this article, a panchromatic (PAN) image is used as an example. Texture features of land-cover types in a PAN image of size $R \times C$ vary greatly in sharpness, brightness, and regularity due to illumination variations. To mitigate the effect of illumination on texture feature analysis, a local texture binary code (LTBC) was proposed using the local binary pattern operator (Qian *et al.* 2011; Liu *et al.* 2016; Liu and Ma. 2022), which was used to redescribe the image data and create an LTBC image. In the LTBC image, the textures of land-cover types are distinctively and identically reflected, affording texture feature analysis7.

Local Texture Binary Code

In a 3 × 3 window centered on pixel $S(S = 1 \dots R \times C)$, LTBC compares the spectral median with the spectral features of the adjacent pixels in this window and provides the corresponding binary codes of the adjacent pixels based on the comparison results:

$$b_k = \begin{cases} 1 & (v_k > mid_v) \\ 0 & (v_k \le mid_v) \end{cases} \tag{1}$$

where b_k is the binary code of the k^{th} ($k = 1 \dots 8$, $k \ne S$) pixel adjacent to pixel S within the window, v_k is the spectral feature of the i^{th} adjacent pixel around pixel S, and mid_v is the spectral median of the window. For example, in a 3×3 window, the spectral features of its adjacent pixels $v_1 \sim v_8$ around pixel S are 9, 62, 89, 6, 9, 100, 87, and 101. Then, the spectral feature of pixel S v_S is (Figure 1a), and the spectral median within the window is 62 ($mid_v = 62$), and the binary codes of the adjacent pixels v_1 to v_8 are obtained through the LTBC definition (Figure 1b). Moreover, the binary codes of v_1 to v_8 are arranged clockwise to obtain the $LTBC_S$ on the central pixel S (Figure 1c). The LTBC definition demonstrates that it solely refers to the spectral features of the pixels within a localized area but not to the pixels of other areas. Therefore, the changes in lighting in different regions have almost no effect on the calculation process of LTBC. This allows for a clear presentation of texture features of ground objects in areas with different lighting intensities in LTBC images, which is the basis for subsequent textures. Thus, edge feature extraction work provides a good data source.

To demonstrate that the textures of land-cover types can be distinctively and identically reflected in the LTBC image, we use LTBC to redescribe the PAN images of the six land-cover types provided in Figure 2a, 2c, 2e, 2g, 2i, and 2k: cultivated land, water, forest, grassland, bare soil, and sand. The corresponding LTBC images are depicted in Figures 2b, 2d, 2f, 2h, 2j, and 2l. Under different illumination, the textures on six land-cover types in the PAN images differ significantly in sharpness and brightness. Meanwhile, in the LTBC images, the influence of illumination is eliminated, and the sharpness and brightness of the textures on six land-cover types have been enhanced. To further prove that the LTBC can effectively enhance the textures’ sharpness, significance, and regularity, the two indexes (i.e., angular second moment [ASM] and contrast) of the GLCM were used to evaluate the texture features of six land-cover types quantitatively. The ASM index reflects whether the changes in texture features are regular, and the larger the ASM value, the more regular the changes in texture features. The contrast index reflects the clarity and saliency of texture features, and the higher its value, the clearer and more obvious the texture features. The evaluation results are displayed in Figure 3. Compared to the evaluation results of PAN images, the ASM on the texture features of six land-cover types increased to a certain degree in the LTBC images, indicating that the texture features became more regular. Meanwhile, the contrast of texture features of six land-cover types increased significantly, inferring that the sharpness and significance of the LTBC images improved significantly. In short, the LTBC image is more suitable for texture feature analysis than the PAN image.

Pixel Texture Index and Its Algorithm

After obtaining the LTBC images, the pixel texture index is proposed to evaluate the context of the texture features between each pixel and its adjacent pixels based on the LTBC image data. Since the LTBC data of the pixels within the same land-cover type are similar, this similarity is used to describe the context of texture features between the pixels. Thus, PTI reflects the homogeneity of texture features within the same land-cover type. Furthermore, the PTI image highlights the edges of different land-cover types, including the growth of direction lines and the calculation of PTI_S.

Growth of Direction Lines

In a circular window centered on pixel $S(S = 1 \dots\dots R \times C)$, eight rays (i.e., direction lines) are independently extended in eight directions from pixel S, with each direction having a length determined by the number of pixels on the direction line. This article uses the similarity

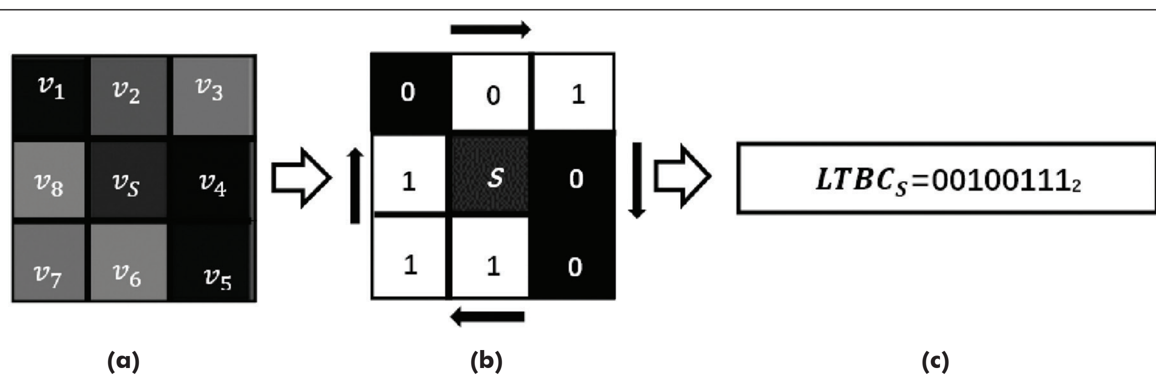

Figure 1. Flow chart of $LTBC_S$. (a) Diagram of the window. (b) Binary code of the window. (c) $LTBC_S$ on central pixel S. LTBC = local texture binary code.

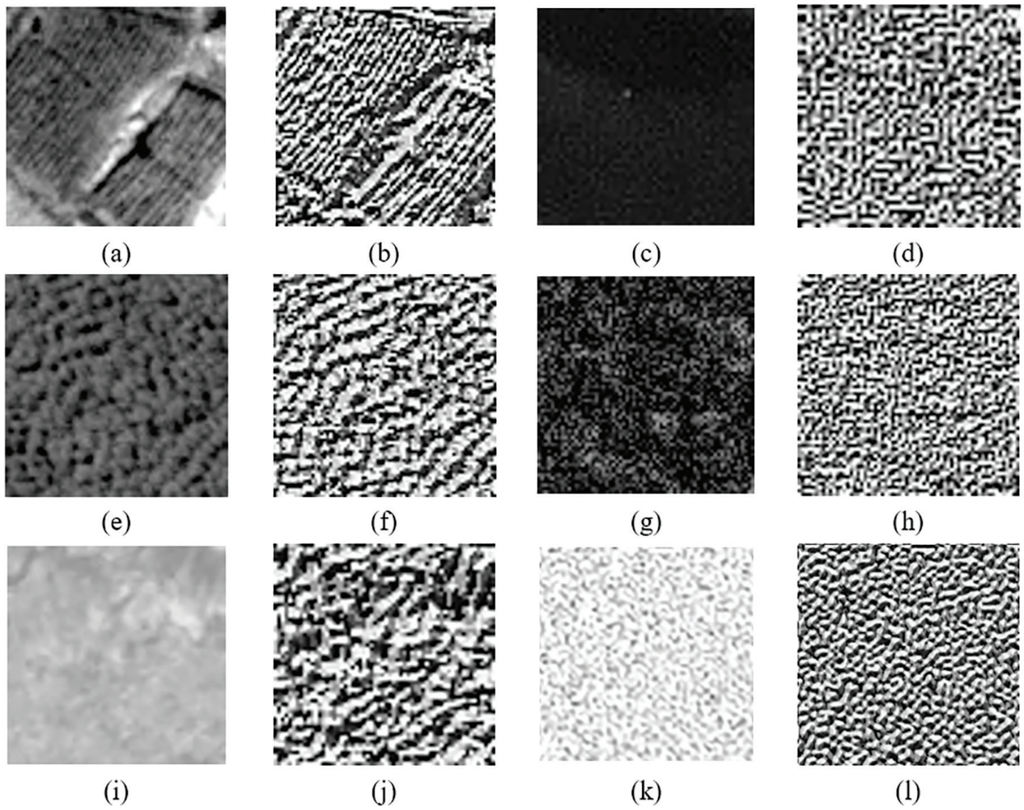

Figure 2. Panchromatic (PAN) images and corresponding local texture binary code (LTBC) images on six land-cover types. (a, c, e, g, i, k) PAN images on cultivated land (a), water (c), forest (e), grassland (g), bare soil (i), sand (*k*). (b, d, f, h, j, l) Corresponding LTBC images on cultivated land (b), water (d), forest (f), grassland (h), bare soil (j), and sand (l).

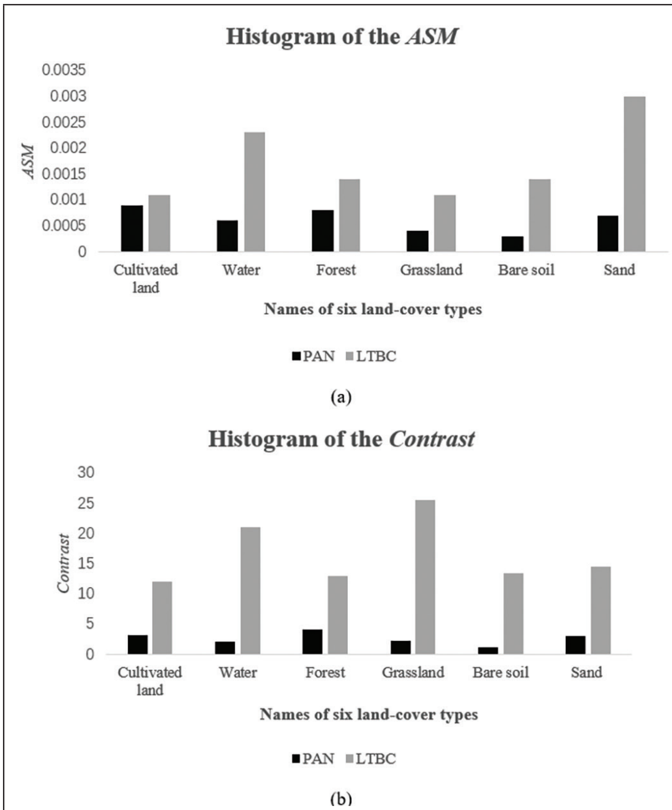

Figure 3. Angular second moment (ASM) and contrast on the texture features of six land-cover types. (a) Histogram of ASM. (b) Histogram of contrast. LTBC = local texture binary code; PAN = panchromatic.

between two LTBC pixel values to describe the homogeneity of texture features between pixels. The more similar the LTBC values of the two pixels, the higher the homogeneity of texture features between the two pixels. The homogeneities of texture features between the pixels along the eight directions are proportional to the lengths of the eight direction lines in the window (Figure 4). SIM_S^i represents the homogeneities of texture features between the central pixel S and its adjacent pixels on the i^{th} (i = 1, 2 … 8) direction line. SIM_S^i is defined as follows:

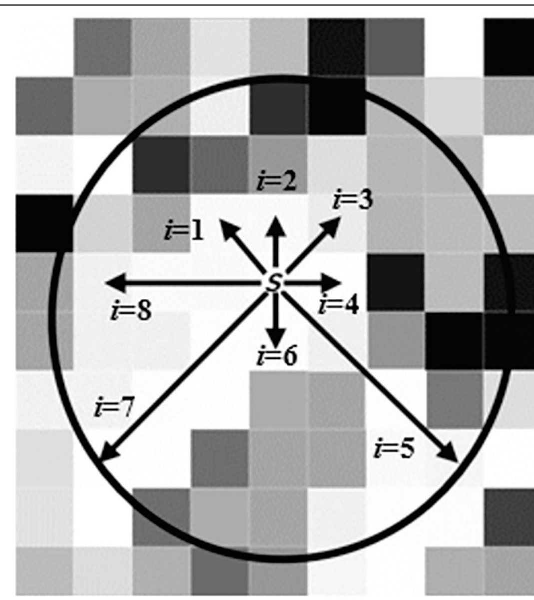

Figure 4. Schematic diagram of eight direction lines from the central pixel *S*.

$$SIM_S^i = LTBC_S \odot LTBC_g^i \tag{2}$$

where $LTBC_S$ represents the LTBC of the central pixel S, $LTBC_g^i$ is the LTBC of an adjacent pixel g on the i^{th} direction line, and $\odot$ represents the *XNOR* bit operation, such as $1 \odot 1 = 1$, $0 \odot 0 = 1$, $1 \odot 0 = 0$, $0 \odot 1 = 0$. Assuming that $LTBC_S = 01101110$ and $LTBC_g^i = 10001101$, $SIM_S^i = LTBC_S \odot LTBC_g^i = 01101110 \odot 10001101 = 00011100$. Hence, the more the number "1" digits in SIM_S^i, the more similar the LTBC values of pixel S and its adjacent pixel g. Therefore, the number of digits "1" in SIM_S^i can be used as a criterion to measure the texture feature similarity between pixel S and its adjacent pixel g, which can determine whether the i^{th} direction line continues to grow. If the digit "1" in SIM_S^i is greater than or equal to a preset threshold T_1, the i^{th} direction line continues to grow until either the digit "1" in SIM_S^i is less than T_1 or the length of i^{th} direction line exceeds the preset threshold T_2.

Calculation of PTI

After generating all direction lines surrounding the central pixel S, the texture index PTI_S of the central pixel S is obtained by simply calculating the lengths of the direction lines. To ensure the rationality of PTI_S on the central pixel S, PTI_S is the weighted sum of the lengths of all direction lines (Equation 3), which is normalized into [0, 255] (Equation 4):

$$PTI'_S = \sum_{i=1}^{N} l_S^i \times \frac{f\left(l_S^i\right)}{\sum_{i=1}^{N} f\left(l_S^i\right)} \tag{3}$$

$$PTI_S = \frac{PTI'_S - PTI'_{min}}{PTI'_{max} - PTI'_{min}} \times 255 \tag{4}$$

where $f(\cdot)$ represents the occurrence frequency of the length value in the set of length values, PTI'_{max} and PTI'_{min} are the maximum and minimum values in PTI data, and l_S^i is the length of the i^{th} direction line, defined as the following Euclidean distance:

$$l_S^i = \sqrt{\left(x_{end}^i - x_S\right)^2 + \left(y_{end}^i - y_S\right)^2} \tag{5}$$

where x_{end}^i and y_{end}^i represent the horizontal and vertical coordinates of the pixel at the end of the i^{th} direction line, and x_S and y_S represent the horizontal and vertical coordinates of the central pixel S. Specifically, if the i^{th} direction line does not grow, $l_S^i = 0$. The PTI process is formally presented in Algorithm 1.

When using the PTI algorithm to describe texture features in LTBC images from the perspective of pixels, the threshold $T_2(T_2 \geq 2)$ determines the maximum length of each directional line. Threshold

Algorithm 1. PTI

```
Date: Ready-for-analysis LTBC image LTBC_{R×C}
Date: Threshold T1(1≤T1≤8)
Date: Threshold T2(T2≥2)
Result: PTI image PTI_{R×C}
Begin:
  for each S = 1 : R×C do
    for each i = 1 : N do
      j = 1
      SIM_S^i = LTBC_S ⊙ LTBC_g^i (Equation 2)
      if SIM_S^i ≥ T1 and j ≤ T2 then:
        j+ = 1
      else:
        l_S^i = sqrt((x_end^i − x_S)^2 + (y_end^i − y_S)^2) (Equation 5)
    PTI'_S = Σ_{i=1}^{N} l_S^i × f(l_S^i) / Σ_{i=1}^{N} f(l_S^i) (Equation 3)
  for each S = 1 : R × C do
    PTI_S = (PTI'_S − PTI'_min) / (PTI'_max − PTI'_min) × 255 (Equation 4)
Return PTI_{R×C}
```

$T_1(1 \leq T_1 \leq 8)$ determines whether the central pixel and its adjacent pixels have similar texture features and whether each direction line continues to expand. Therefore, whether the settings of T_1 and T_2 are reasonable and will directly affect the quality of PTI image data should be explored further.

Settings of Thresholds T_1 and T_2

In order to propose a reasonable method for setting thresholds T_1 and T_2, we select a PAN image of IKONOS as the experimental area (Figure 5a). The experimental area image has a size of 281 255 pixels and a spatial resolution of 1 m, depicting water, bare soil, forest, and cultivated land. However, we redescribe the experimental area using LTBC to eliminate the illumination influence on the texture feature analysis, in which the corresponding LTBC image (Figure 5b) presents high-resolution texture features of different land-cover types. Subsequently, it is very important to determine reasonable thresholds T_1 and T_2 before the PTI image is obtained based on the LTBC image (Figure 5b) using the PTI algorithm (see "Calculation of PTI"). Due to the noncorrelation between thresholds T_1 and T_2, the argumentation process regarding the reasonable values of T_1 and T_2 can be discussed separately and independently.

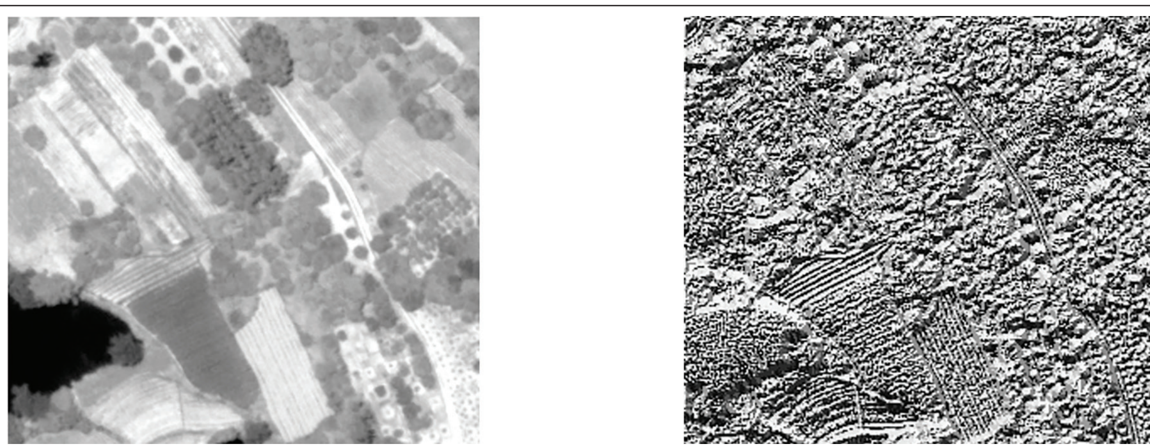

(a) (b)

Figure 5. Panchromatic (PAN) image and experimental data of the experimental area. (a) PAN image. (b) Local texture binary code (LTBC) image.

I_{PTI} Index

In the PTI image, if the PTI of different land-cover types is more discrete and the PTI of the same land-cover type is more cohesive, then the PTI image is more suitable for image segmentation. Hence, the indicator I_{PTI} is proposed, which is directly proportional to the dispersion of PTI about interclass pixels and inversely proportional to the dispersion of PTI about intraclass pixels. The higher the I_{PTI} value, the better the quality of PTI image data. The sum of the absolute values of the difference in the mean values about PTI of each land-cover type sample represents the dispersion of PTI about interclass pixels. The sum of the absolute values of the difference between the PTI of each sample pixel and the mean value about PTI of the sample pixels in the same land-cover type represents the dispersion of PTI about intraclass pixels. The calculation formula is as follows:

$$I_{\mathrm{PTI}} = \frac{\left(\sum_{k=1,k\neq j}^{N} \left| \mu_j - \mu_k \right|\right)}{\left(\sum_{j=1}^{N} \sum_{i=1}^{M} \left| \mathrm{PTI}_j^i - \mu_j \right|\right)}) \quad (6)$$

where N is the total of land-cover types in the image, M is the total of sample pixels in each land-cover type, μ_j represents the mean value about PTI of the sample pixels in the j^{th} land-cover type, $\mu_k(k \neq j)$ represents the mean value of PTI of the sample pixels in the k^{th} land-cover type, and PTI_j^i represents the PTI of the i^{th} sample pixel in the j^{th} land-cover type.

Settings of T_1 and T_2

From the image in Figure 5a, 50 sample pixels were collected from each land-cover type using random sampling. Assuming threshold T_2 was temporarily set to 10, we calculated the corresponding I_{PTI} when T_1 increased from 1 to 8. The line chart of Figure 6a reflects the relationship between I_{PTI} and T_1, highlighting that when T_1= 6, I_{PTI} maximizes; thus, T_1 = 6 is reasonable.

When T_1 = 6, the corresponding I_{PTI} was calculated when T_2 increased from 2 to 20. The line chart of Figure 6b reflects the relationship between I_{PTI} and T_2 (when T_1 = 6), revealing that for T_2 = 5, I_{PTI} maximizes, and therefore T_2 = 5 is a reasonable value.

Based on the above experimental results, T_1 is set to 6, and T_2 is set to 5. Based on the LTBC image (Figure 5b), the PTI algorithm (see "Calculation of PTI") is used to obtain the PTI image (Figure 7a). Finally, the image of the experimental area is segmented using Definiens Developer software, with the segmental scale set to 60. The other segmentation parameters use the default values. Compared with the segmental result of the PAN image (Figure 7b), the "oversegmentation" and "undersegmentation" phenomena are significantly reduced by combining PAN and PTI images (Figure 7c), thus improving the segmentation quality, almost reflecting the land use situation.

Experiments

To avoid the contingency in the abovementioned experiments and verify the superiority and robustness of the proposed PTI algorithm, two experimental areas were selected from two distinct types of HSRRS images. Figure 8 depicts the experimental procedure, with the corresponding experiments demonstrating that the PTI image can effectively improve the image classification and segmentation quality. The first experimental area was selected from the QuickBird, with Figure 9 depicting the original and the corresponding LTBC images of all bands. The multi-spectral (i.e., blue [450 to 520 nm], green [520 to 600 nm], red [630 to 690 nm], and near-infrared [NIR, 760 to 900 nm]) images of this experimental area are 211 × 181 pixels, and the spatial resolution is 2.44 m. The PAN (610 to 720 nm) image of this

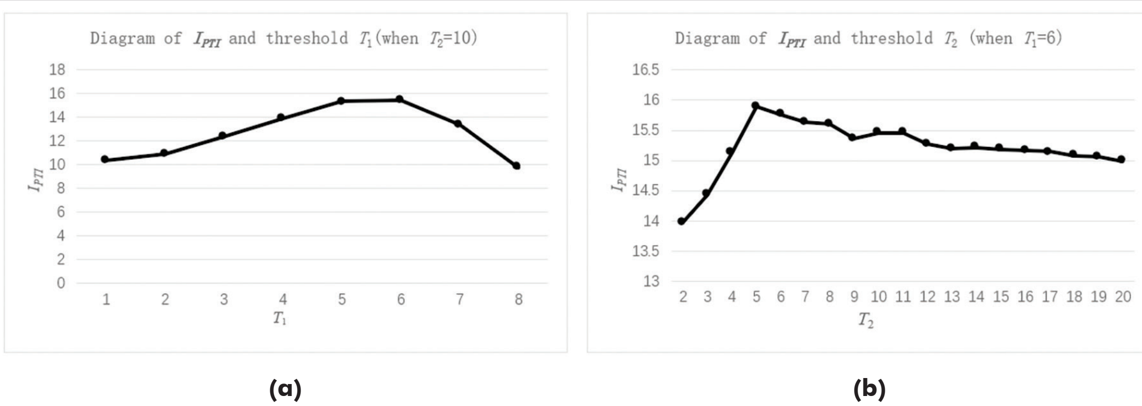

Figure 6. Calculation results of I_{PTI}. (a) Relationship between I_{PTI} and T_1(when T_2 = 10). (b) Relationship between I_{PTI} and T_2 (when T_1 = 6. PTI = pixel texture index.

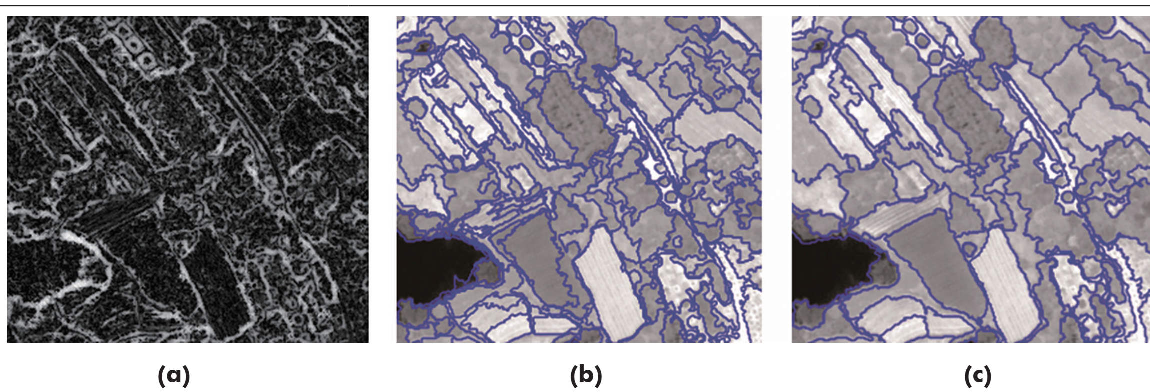

Figure 7. Panchromatic (PAN) image and experimental data of the experimental area. (a) Pixel texture index (PTI) image. (b) Segmental result based on PAN image. (c) Segmental result by combining PAN image with PTI image.

experimental area is 792 × 734 pixels, and the spatial resolution is 0.61 m, presenting artificial land-cover types and noise (such as shadow).

The second experimental area was selected from the WorldView-II. The Coastal-band (400 to 450 nm), yellow (585 to 625 nm), red-edge (705 to 745 nm), and NIR-II (860 to 1040 nm) images provided by WorldView-II are specifically used for vegetation identification and analysis. The images of the four bands were selected for this experiment because vegetation is the main land-cover type of the second experimental area. The original and corresponding LTBC images of all bands are illustrated in Figure 10. The multi-spectral images of this experimental area are 141 × 131 pixels, and the spatial resolution is 1.8 m. The PAN (450 to 800 nm) image of this experimental area

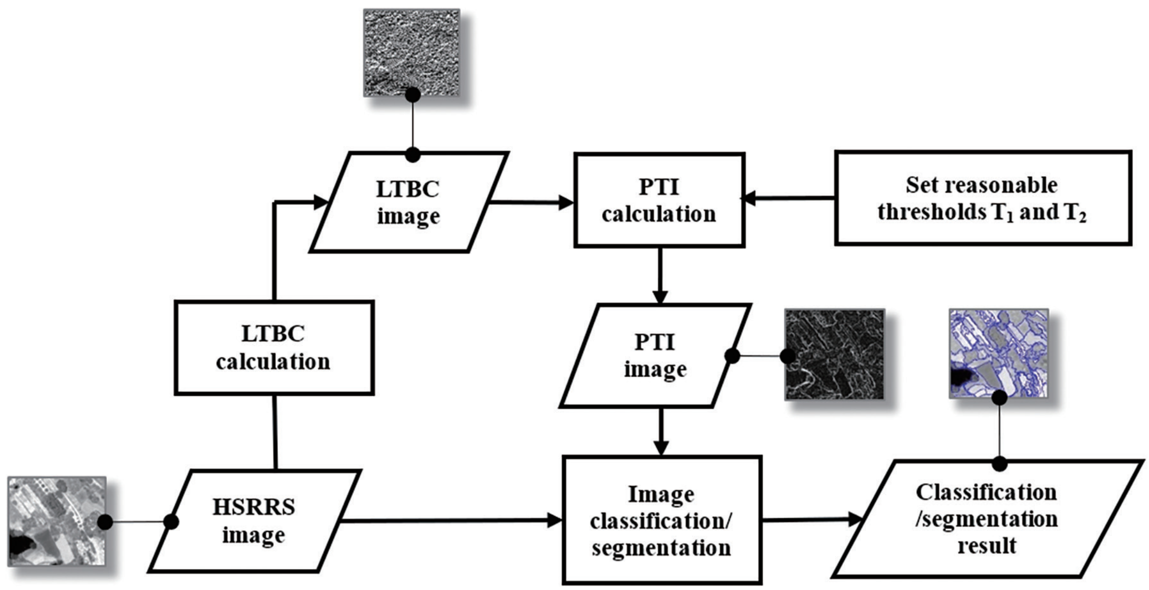

Figure 8. Flow chart of the experimental procedure. HSRRS = high spatial resolution remotely sensed; LTBC = local texture binary code; PTI = pixel texture index.

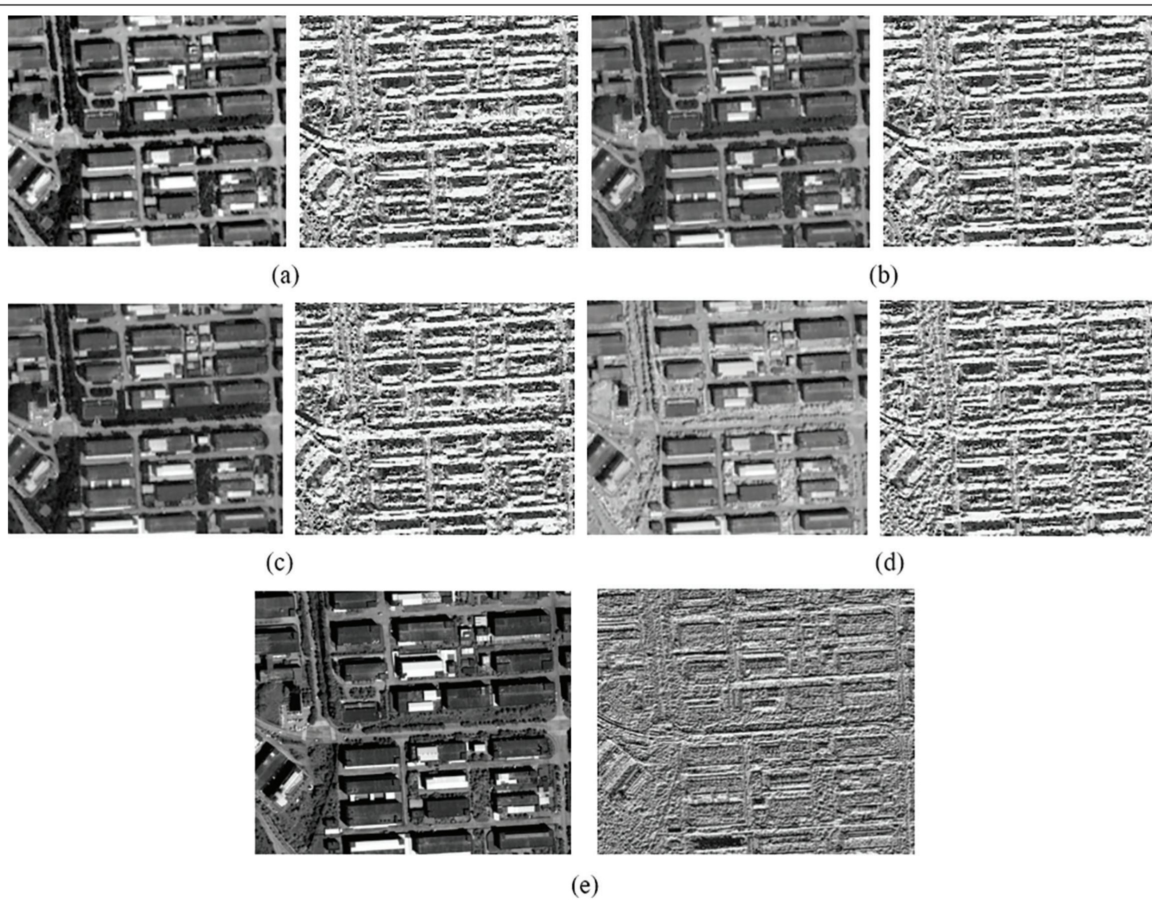

Figure 9. High spatial resolution remotely sensed (HSRRS) images and the corresponding local texture binary code (LTBC) images of the first experimental area. (a) Blue image and corresponding LTBC image. (b) Green image and corresponding LTBC image. (c) Red image and corresponding LTBC image. (d) Near-infrared (NIR) image and corresponding LTBC image. (e) PAN image and corresponding LTBC image.

image is 561 × 524 pixels with a spatial resolution of 0.5 m, presenting cultivated land, forest, water, and bare soil. The two experimental areas reflect two distinct land use situations.

Since multi-spectral images have multi-dimensional spectral features, these images are suitable for classification experiment. Specifically, it is suitable for segmental experiment based on a single spectral feature provided by PAN image. This article verifies the PTI algorithm's superiority and robustness from classification of multi-spectral images and segmentation of PAN images.

Classifications of Multi-spectral Images

Firstly, classification experiments of multi-spectral images were performed. Before deriving the PTI images, the I_{PTI} (see "I_{PTI} Index") was used to determine the reasonable values of the thresholds T_1 and T_2. Using random sampling, 40 sample pixels were collected from each land-cover type of the two experimental areas. The threshold T_2 of the first experimental area was temporarily set to 15, the threshold T_2 of the second experimental area was temporarily set to 10, and the corresponding I_{PTI} (Equation 6) was calculated when T_1 increased from 1 to 8. Figures 11a and 12a illustrate the relationship between I_{PTI} and T_1 about the two experimental areas. In Figure 11a, due to the high

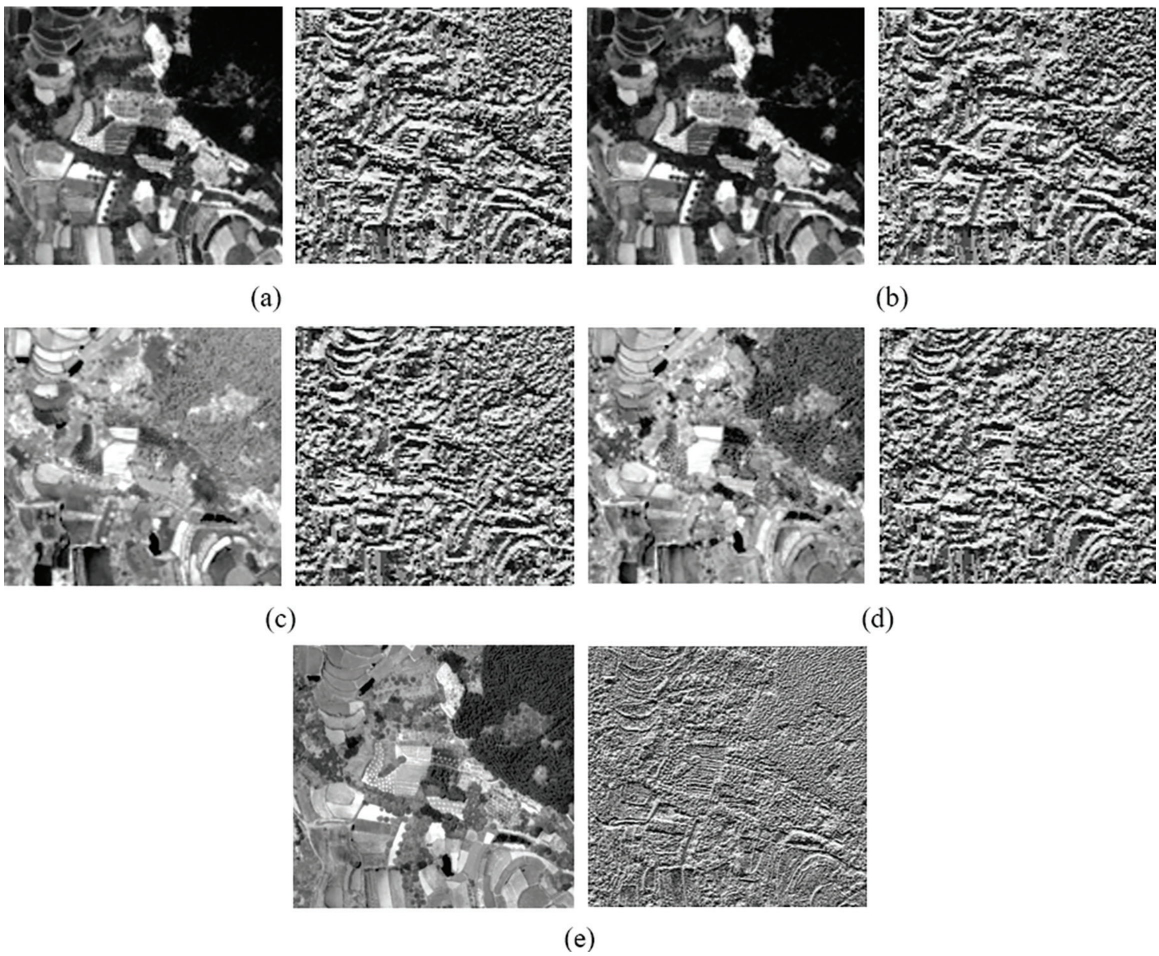

Figure 10. High spatial resolution remotely sensed (HSRRS) images and the corresponding local texture binary code (LTBC) images of the second experimental area. (a) Coastal-band image and corresponding LTBC image. (b) Yellow image and corresponding LTBC image. (c) Near-infrared II (NIR-II) image and corresponding LTBC image. (d) Red-edge image and the corresponding LTBC image. (e) PAN image and corresponding LTBC image.

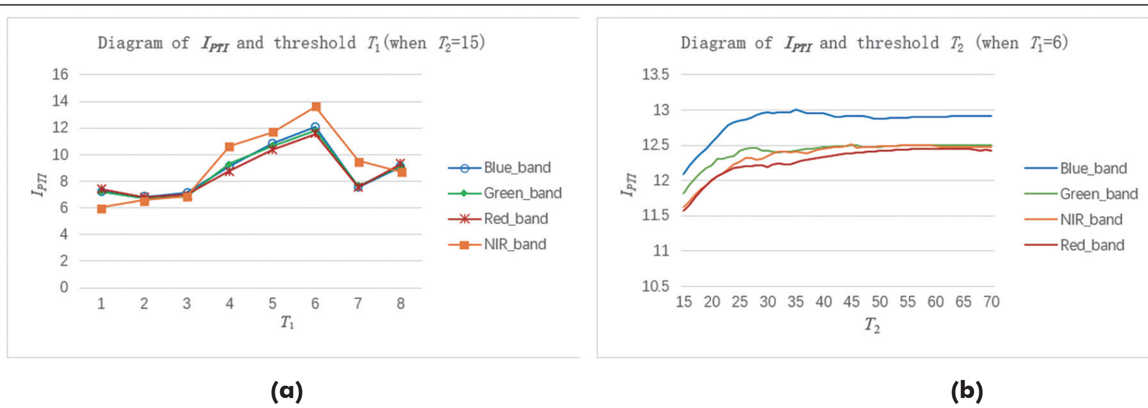

Figure 11. Calculation results of I_{PTI} of the first experimental area about multi-spectral images. (a) Relationship between I_{PTI} and T_1 (when T_2 = 15). (b) Relationship between I_{PTI} and T_2 (when T_1 = 6). NIR = near-infrared; PTI = pixel texture index.

correlation of the data between visual bands (i.e., blue, green, red), the trends of I_{PTI} about the sample points in visual bands are similar. However, the correlation between the NIR band and visible bands is not high, so there is a significant difference in the trend of I_{PTI} about the sample points in NIR bands compared to the former. When $T_1 = 6$, I_{PTI} maximizes, and therefore, the reasonable value of T_1 is 6 for the first experimental area. In Figure 12a, due to the high correlation between Coastal-band and yellow, the trends of I_{PTI} about the sample points in the two bands are similar. The correlation between red-edge and NIR-II is relatively high, so the trends of I_{PTI} about the sample points in the two bands are similar. When $T_1 = 7$, I_{PTI} maximizes, and therefore, the reasonable value of T_1 is 7 for the second experimental area.

For the first experimental area, we considered $T_1 = 6$, and the corresponding I_{PTI} was calculated while T_2 increased from 15 to 70. Figure 11b depicts the relationship between I_{PTI} and T_2, suggesting that when T_2= 35, 46, 63, and 45, I_{PTI} in blue, green, red, and NIR maximizes, respectively. When T_2 exceeds these values, I_{PTI} decreases and then tends to stabilize. Therefore, the reasonable values of T_2 in four bands are 35, 46, 63, and 45. Based on the thresholds T_1 and T_2 calculated above, we derived PTI images (Figure 13) from the LTBC images (Figure 9a–d) using the PTI algorithm (see "Calculation of PTI"). For the second experimental area $T_1 = 7$, and the corresponding I_{PTI} was calculated, while T_2 increased from 5 to 33. Figure 12b depicts the relationship between I_{PTI} and T_2, suggesting that when $T_2 = 24$, 24, 25, and 26, I_{PTI} in Coastal-band, yellow, red-edge, and NIR-II maximizes, respectively. When T_2 exceeds these values, I_{PTI} slightly decreases and tends to stabilize finally. Therefore, the reasonable values of T_2 in four bands are 24, 24, 25, and 26. Based on the T_1 and T_2 thresholds calculated above, we derived PTI images (Figure 14) from the LTBC images (Figure 10a–d) using the PTI algorithm (see "Calculation of PTI"). The homogeneity of each land-cover type's texture features and each land-cover type's edges is presented in the PTI images of all bands.

Correlation analysis was performed between the multi-spectral and PTI images of the two experimental areas to obtain the correlation coefficient matrixes. Tables 1 and 2 highlight that the correlation between PTI images and the multi-spectral images is very low. This statistic indicates that the information redundancy between PTI and multi-spectral images is very low. It describes the various land-cover types' high frequency, which increases the dimension of the image classification feature space and provides effective data support for improving classification accuracy.

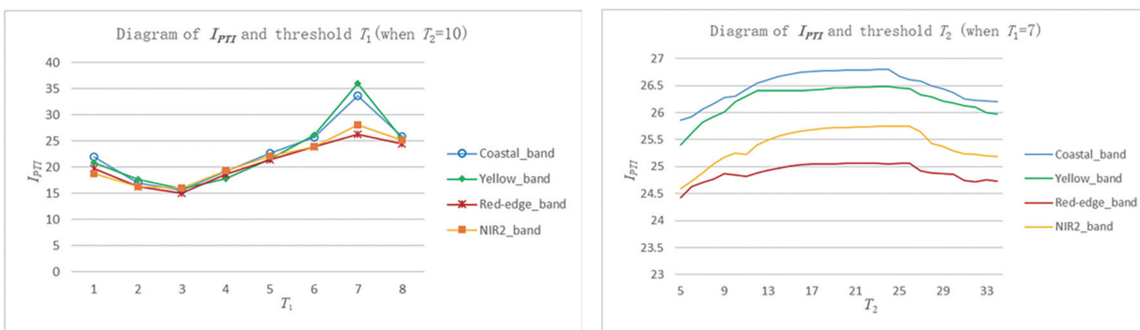

(a) (b)

Figure 12. Calculation results of I_{PTI} of the second experimental area about multi-spectral images. (a) Relationship between I_{PTI} and T_1 (when T_2 =10). (b) Relationship between I_{PTI} and T_2 (when $T_1 = 7$). NIR2 = near-infrared II; PTI = pixel texture index.

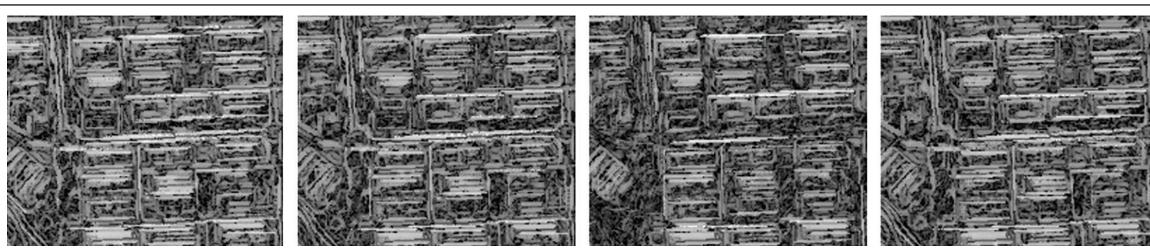

(a) (b) (c) (d)

Figure 13. Pixel texture index (PTI) images of the first experimental area about multi-spectral images. (a) PTIBlue image. (b) PTIGreen image. (c) PTI_{Red} image. (d) PTI_{NIR} image.

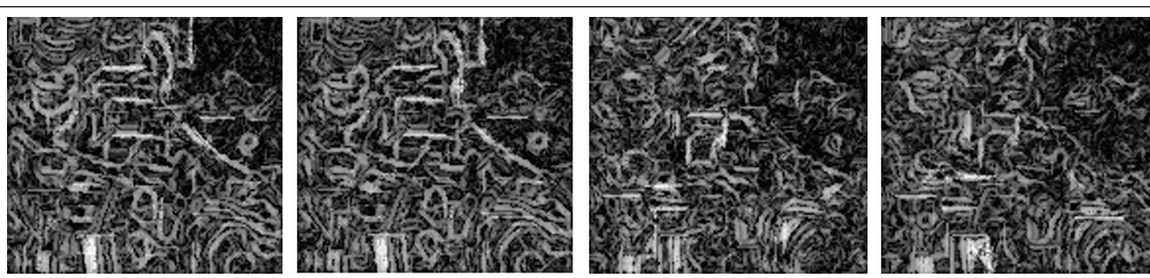

(a) (b) (c) (d)

Figure 14. Pixel texture index (PTI) images of the second experimental area about multi-spectral images. (a) $PTI_{Coastal\text{-}band}$ image. (b) PTIYellow image. (c) $PTI_{Red\text{-}edge}$ image. and (d) $PTI_{NIR\text{-}II}$ image.

In order to verify the effect of PTI image data on image classification, a simple supervised classification technique was adopted to classify the land-cover types of the two experimental areas into five categories. The classification of each experimental area was performed twice. The first classification was executed based on multi-spectral images, referred to as data 1. The second classification was executed by combining low-correlation multi-spectral images and PTI images, referred to as data 2. Data 2 of the first experimental area included red, NIR, PTI_{Red}, PTI_{NIR}, and Data 2 of the second experimental area included yellow, red-edge, NIR-II, $PTI_{Coastal\text{-}band}$, $PTI_{Red\text{-}edge}$, $PTI_{NIR\text{-}II}$. Additionally, to evaluate the classification results, the PAN images of the experimental area were used as references; combined with the actual land use situation, manual mapping was used to obtain the correct classification results (Figures 15a and 16a). The classification results of the two experimental areas are depicted in Figures 15b, 15c, 16b, and 16c.

Segmentations of PAN Images

Subsequently, segmental experiments of PAN images were performed. Specifically, using random sampling, 70 sample pixels were collected from each land-cover type for the first experimental area. The threshold T_2 was temporarily set to 60, and the corresponding I_{PTI} (Equation

Table 1. Correlation coefficient matrix of the eight bands about the first experimental area.

Correlation coefficient	**Blue**	**Green**	**Red**	**NIR**	**PTI_{Blue}**	**PTI_{Green}**	**PTI_{Red}**	**PTI_{NIR}**
Blue	1.000	0.990	0.955	0.584	−0.003	−0.003	0.016	0.018
Green	0.990	1.000	0.980	0.599	−0.002	−0.003	0.018	0.012
Red	0.955	0.980	1.000	0.553	0.006	0.003	0.018	0.024
NIR	0.584	0.599	0.553	1.000	−0.114	−0.100	−0.062	−0.247
PTIBlue	−0.003	−0.002	0.006	−0.114	1.000	0.867	0.800	0.506
PTIGreen	−0.003	−0.003	0.003	−0.100	0.867	1.000	0.813	0.508
PTIRed	0.016	0.018	0.018	−0.062	0.800	0.813	1.000	0.445
PTINIR	0.018	0.012	0.024	−0.247	0.506	0.508	0.445	1.000

NIR = near-infrared; PTI = pixel texture index.

Table 2. Correlation coefficient matrix of the eight bands about the second experimental area.

Correlation coefficient	**Coastal-band**	**Yellow**	**Red-edge**	**NIR-II**	**$PTI_{Coastal\text{-}band}$**	**PTI_{Yellow}**	**$PTI_{Red\text{-}edge}$**	**$PTI_{NIR\text{-}II}$**
Coastal-band	1.000	0.989	0.348	−0.333	0.147	0.191	0.140	0.170
Yellow	0.989	1.000	0.278	−0.376	0.150	0.200	0.141	0.179
Red-edge	0.348	0.278	1.000	0.714	0.026	0.019	0.021	−0.004
NIR-II	−0.333	−0.376	0.714	1.000	−0.079	−0.115	−0.071	−0.132
PTICoastal-band	0.147	0.150	0.026	−0.079	1.000	0.703	0.255	0.273
PTIYellow	0.191	0.200	0.019	−0.115	0.703	1.000	0.249	0.299
PTIRed-edge	0.140	0.141	0.021	−0.071	0.255	0.249	1.000	0.400
PTINIR-II	0.170	0.179	−0.004	−0.132	0.273	0.299	0.400	1.000

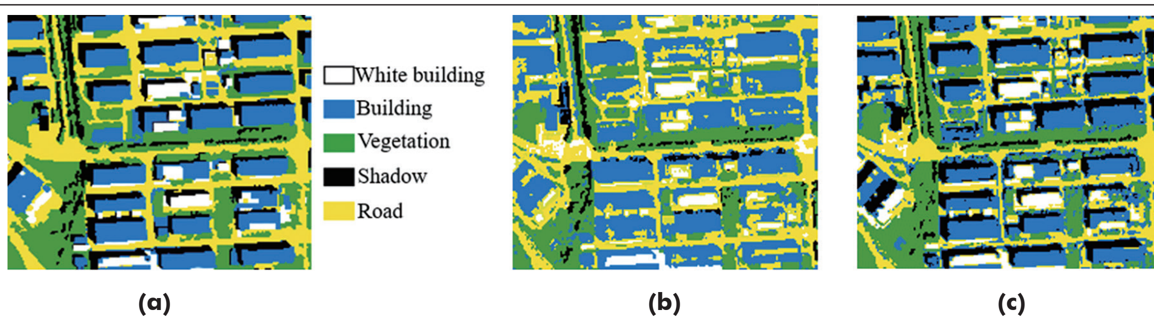

Figure 15. Experimental results of the first experimental area about multi-spectral images. (a) Manually corrected classification result. (b) Classification result based on data 1. (c) Classification result based on data 2.

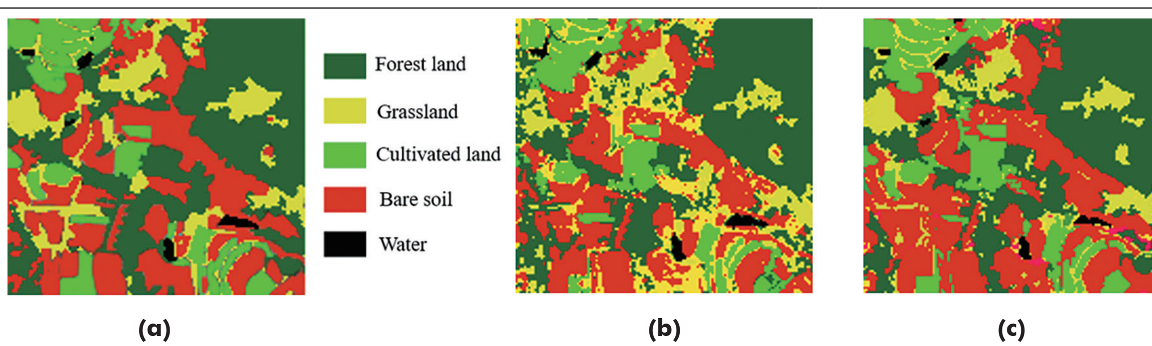

Figure 16. Experimental results of the second experimental area about multi-spectral images. (a) Manually corrected classification result. (b) Classification result based on data 1. (c) Classification result based on data 2.

6) was calculated when T_1 increased from 1 to 8. Figure 17a illustrates the relationship between I_{PTI} and T_1, revealing that when $T_1 = 6$, I_{PTI} maximizes, and therefore, the reasonable value of T_1 is 6. Then, for $T_1 = 6$ the corresponding I_{PTI} was calculated, while T_2 increased from 50 to 60. Figure 17b depicts the relationship between I_{PTI} and T_2 , suggesting that when $T_2 = 57$, I_{PTI} maximizes, and therefore, the reasonable value of T_2 is 57.

Second, using random sampling, 60 sample pixels were collected from each land-cover type for the second experimental area. The threshold T_2 was temporarily set to 10. The corresponding I_{PTI} was calculated. When the threshold T_1 increased from 1 to 8, and a line chart was used to reflect the relationship between I_{PTI} and T_1 (Figure 18a). It showed that when $T_1 = 6$, the I_{PTI} reached its maximum therefore the reasonable value of T_1 is 6. When $T_1 = 6$, the corresponding I_{PTI} was calculated when the threshold T_2 increases from 2 to 10, and a line chart is used to reflect the relationship between I_{PTI} and T_2 (Figure 18b). It showed that when $T_2 = 4$, the I_{PTI} reached its maximum; therefore the reasonable value of T_2 is 4.

Based on the thresholds T_1 and T_2 calculated above, we derived PTI images from the LTBC images (Figure 9b and 9d) using the PTI algorithm (see "Calculation of PTI"). The homogeneity of each land-cover type's texture features and each land-cover type's edges is presented in the PTI images (Figure 19).

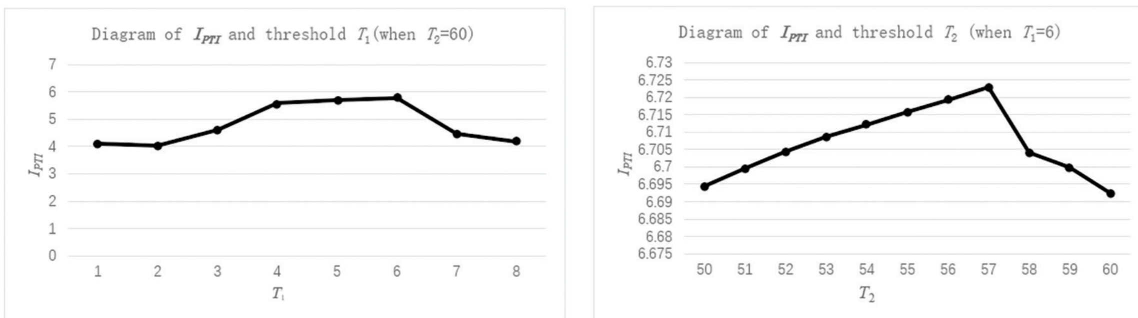

(a) (b)

Figure 17. Calculation results of I_{PTI} of the first experimental area about panchromatic (PAN) image. (a) Relationship between I_{PTI} and T_1 (when $T_2 = 60$. (b) Relationship between I_{PTI} and T_2 (when $T_1 = 6$). PTI = pixel texture index.

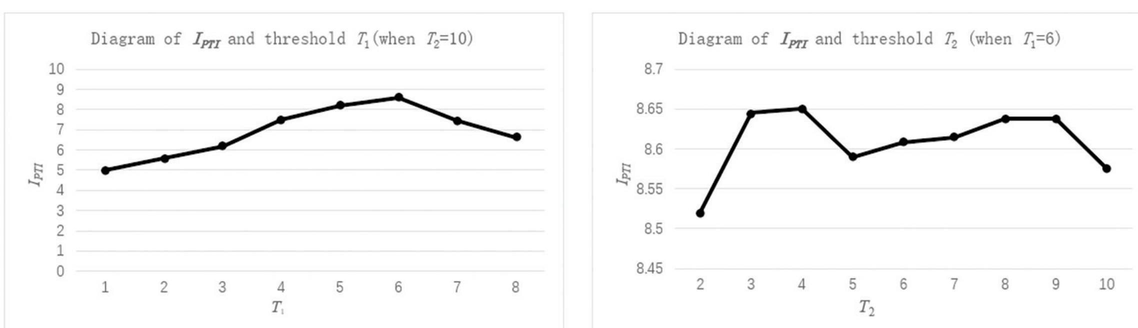

(a) (b)

Figure 18. Calculation results of I_{PTI} of the second experimental area about panchromatic (PAN) image. (a) Relationship between I_{PTI} and T_1 (when $T_2 = 10$). (b) Relationship between I_{PTI} and T_2 (when $T_1 = 6$). PTI = pixel texture index.

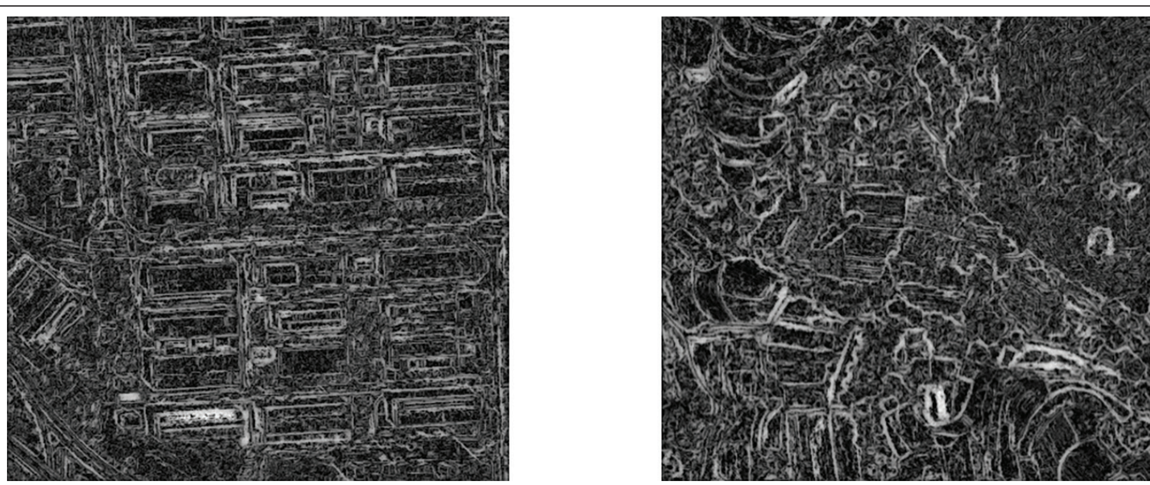

(a) (b)

Figure 19. Pixel texture index (PTI) images of two experimental areas about panchromatic (PAN) images. (a) PTI image of the first experimental area. (b) PTI image of the second experimental area.

The segmentation parameters for the first experiment are a segmentation scale of 150 and a shape factor of 0.3, while the other parameters are the default. Accordingly, the segmentation scale is set to 80 for the second experimental area, and the other parameters are the default. Based on the two data sets, the PAN images of the two experimental areas are segmented twice. The first set of data solely comprises a PAN image (Figures 9e and 10e), referred to as data 1, and the second set consists of PAN images (Figures 9e and 10e) and its PTI images (Figure 19a and 19b), referred to as data 2. The segmentation results are presented in Figure 20, where the blue lines represent the image segmentation-generated contour lines of the objects.

Results and Analysis

We first used manual visual interpretation to analyze and compare the experimental results to ensure the evaluation rationality. Then, we combined classification and segmentation metrics to evaluate the experimental results objectively.

Analysis of Classification Results

The classification results of the two experimental areas were evaluated using manual visual interpretation, the confusion matrix, overall accuracy, and the kappa coefficient.

Manual Visual Interpretation

First, by using manual visual interpretation, the classification results of the two experimental areas were compared. It was found that: (1) In the classification result based on data 1 of the first experimental area, many shadow pixels were misclassified as buildings, while some light-gray building pixels were misclassified as roads, resulting in low classification accuracy of these land-cover types. Meanwhile, due to the interference of traffic line pixels on classification, the completeness of the road was not high in the result. However, in the classification result based on data 2 of the experimental area, the misclassifications between building and shadow and between building and road were significantly reduced, and the completeness of the road was also improved. (2) In the classification result based on data 1 of the second experimental area, some forest pixels were misclassified as grassland, and some grassland pixels were misclassified as cultivated land. Meanwhile, because some bare soil areas are covered with a small amount of vegetation, some pixels were classified as grassland. In the classification result, the bare soil area was incomplete and inconsistent with the land use status. In the classification result based on data 2 of the experimental area, the misclassifications between forest and grassland and between grassland and cultivated land were reduced, and the completeness of the bare soil area significantly improved.

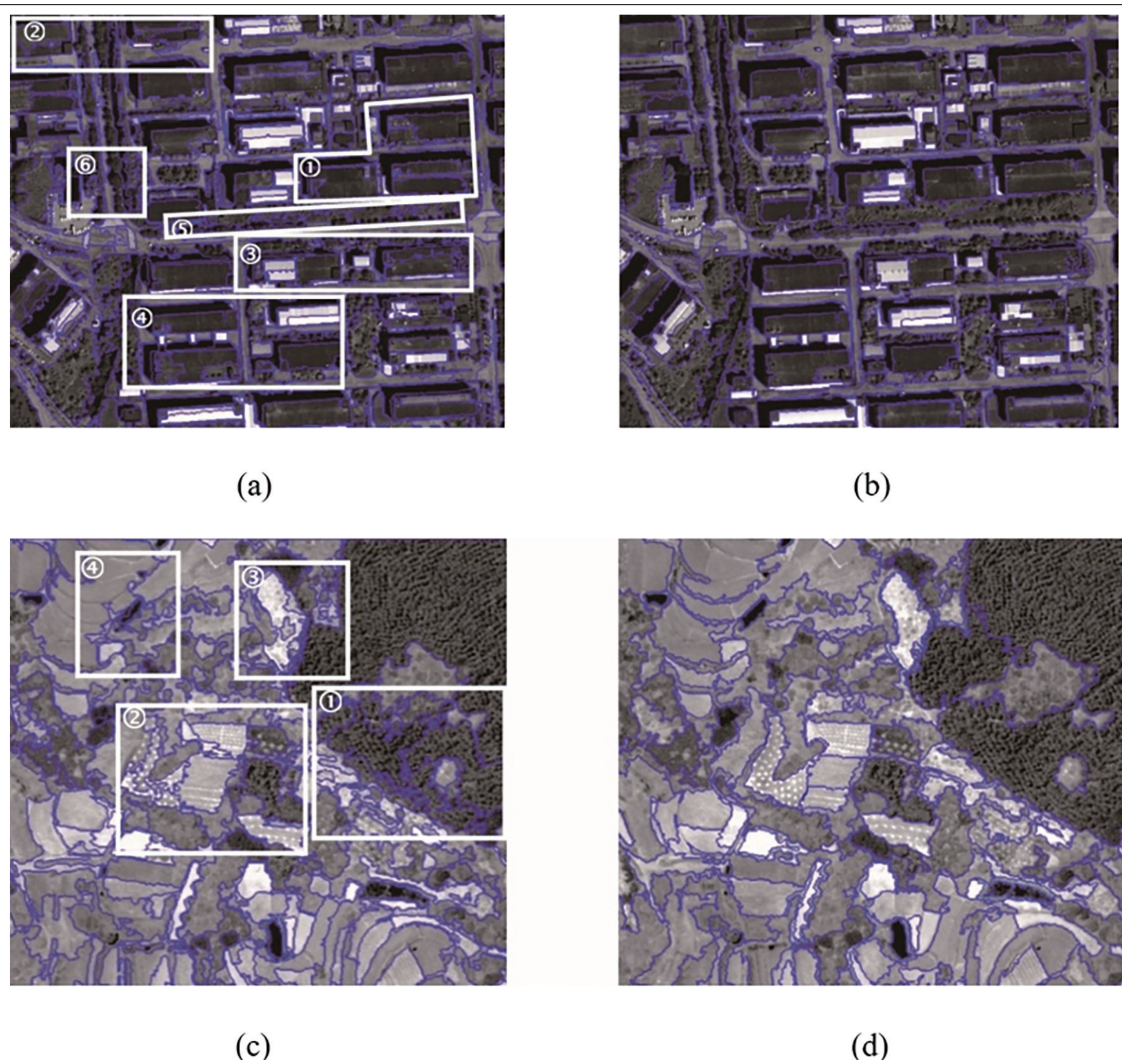

Figure 20. Experimental results of two experimental areas about PAN images. (a) Segmental result of the first experimental area based on data 1. (b) Segmental result of the first experimental area based on data 2. (c) Segmental result of the second experimental area based on data 1. (d) Segmental result of the second experimental area based on data 2.

Accuracy Verification

Secondly, the classification accuracy was verified using the confusion matrix, overall accuracy, and the kappa coefficient. Using the partition random sampling method, 90 validation pixels were extracted from each land-cover type in two experimental areas. Referring to the correct classification results by manually drawing the two experimental areas (Figures 15a and 16a), accuracy verification was carried out through human–computer interaction. The results are reported in Tables 3 and 4, revealing that the overall classification accuracy based on data 2 improved from 7% to 14%, and its kappa coefficient increased from 11% to 24%.

Table 3. Accuracy validation results of the first experimental area.

	Data	White Building	Building	Vegetation	Shadow	Road	Total
Classification result based on Data 1	White building	82	0	0	0	11	93
	Building	0	79	0	47	8	134
	Vegetation	0	0	85	0	2	87
	Shadow	0	0	3	31	2	36
	Road	8	11	2	12	67	100
	Total	90	90	90	90	90	450
	Overall accuracy (%) 76%						
	Kappa 0.71						
Classification result based on Data 2	White building	85	0	0	0	5	90
	Building	0	81	0	4	5	90
	Vegetation	0	0	86	6	2	94
	Shadow	0	4	2	76	1	83
	Road	5	5	2	4	77	93
	Total	90	90	90	90	90	450
	Overall accuracy (%) 90%						
	Kappa 0.88						

Analysis and Evaluation of Classification Results

Through manual visual interpretation and accuracy verification of the data, we found that the classification accuracy based on data 1 is inferior to the classification results based on data 2. This is because, first, for the first experimental area, the spectral values of the pixels of building shadow in blue, red, and green are close to those of the dark-gray buildings. There are significant differences between the spectral values of these pixels in NIR and PTI_{Red}, PTI_{NIR} (Figure 21a). The spectral values of the pixels of light-gray buildings in blue, green, and

Table 4. Accuracy validation results of the second experimental area.

	Data	Forest Land	Grassland	Cultivated Land	Bare Soil	Water	Total
Classification result based on data 1	Forest land	72	0	0	0	0	72
	Grassland	14	71	12	12	0	109
	Cultivated land	0	10	73	0	0	83
	Bare soil	4	6	5	78	0	93
	Water	0	3	0	0	90	93
	Total	90	90	90	90	90	450
	Overall accuracy (%) 85%						
	Kappa 0.82						
Classification result based on data 2	Forest land	80	0	0	0	0	80
	Grassland	8	81	5	4	0	98
	Cultivated land	2	5	82	3	0	92
	Bare soil	0	4	3	83	0	90
	Water	0	0	0	0	90	90
	Total	90	90	90	90	90	450
	Overall accuracy (%) 92%						
	Kappa 0.91						

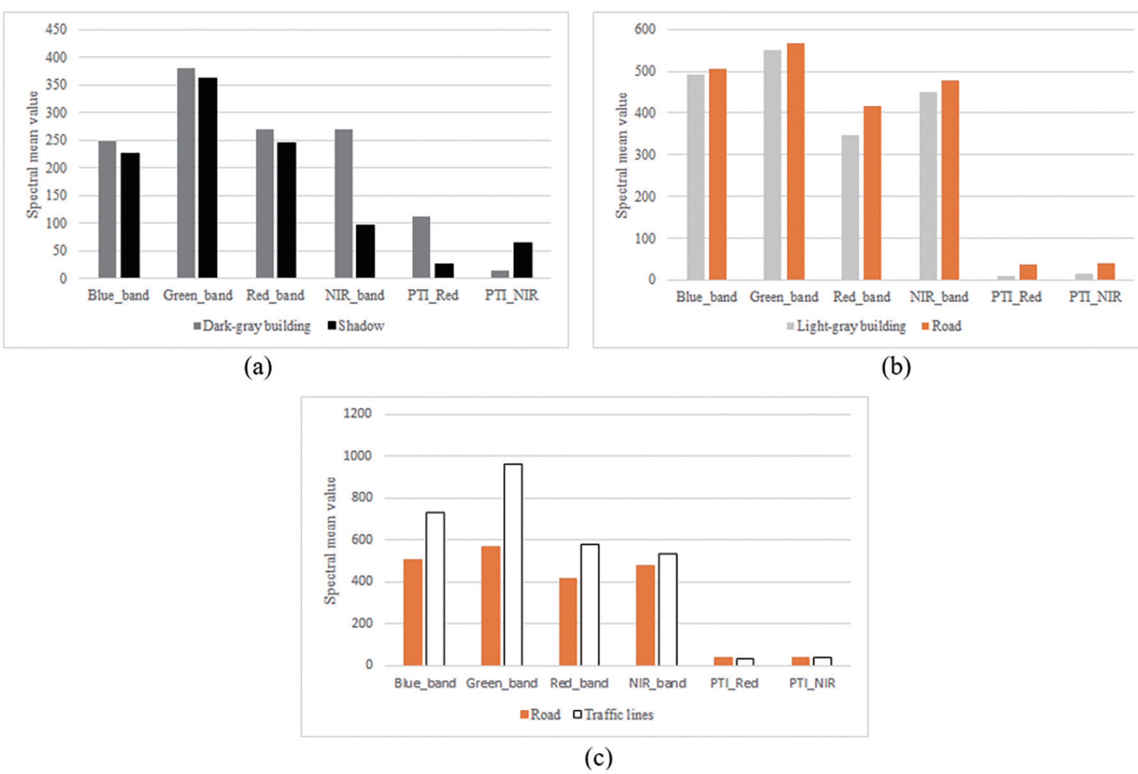

Figure 21. Comparison of spectral mean values of some pixels in the first experimental area about multi-spectral images. (a) Dark-gray building pixels versus shadow pixels. (b) Light-gray building pixels versus road pixels. (c) Road pixels versus traffic lines pixels. NIR = near-infrared; PTI = pixel texture index.

NIR are close to that of the road. In addition, there are significant differences between the spectral values of these pixels in red, PTI_{Red} and PTI_{NIR} (Figure 21b). Therefore, in the classification result based on data 1, many pixels of the building shadow were misclassified as buildings, and some light-gray buildings were misclassified as roads. The classification accuracy of these pixels significantly improved in the classification result based on data 2. Meanwhile, there are significant differences between the spectral values of traffic line pixels in blue, green, and red and the spectral values of road pixels (Figure 21c). After classification, these pixels were classified into nonroad, reducing the road's integrity. However, the spectral values of traffic line pixels in NIR, PTI_{Red} , and PTI_{NIR} are similar to that of the road. Therefore, in the classification result based on data 2, these pixels were classified as roads, improving the integrity of the road.

For the second experimental area, the spectral values of some light-green forest pixels in yellow and red-edge are relatively close to that of grassland pixels, and there are some differences between the spectral values of these pixels in the Coastal-band, NIR-II, $PTI_{Red\text{-}edge}$, $PTI_{NIR\text{-}II}$, and $PTI_{Coastal\text{-}band}$ $PTI_{Coastal\text{-}band}$ (Figure 22a). The spectral values of some grassland pixels in Coastal-band, yellow, and NIR-II are similar to that of cultivated land pixels, and there are some differences between the spectral values of these grassland pixels in red-edge, $PTI_{Red\text{-}edge}$, $PTI_{NIR\text{-}II}$, and $PTI_{Coastal\text{-}band}$ $PTI_{Coastal\text{-}band}$ and that of cultivated land pixels (Figure 22b). The homogeneity of spectral values leads to some light-green forest pixels being misclassified as grasslands and some grassland pixels misclassified as cultivated land in the classification result based on data 1. However, the heterogeneity of spectral features enhances the classification accuracy of these pixels in the classification result based on data 2. The vegetation pixels covering bare soil have significant differences in the spectral values of Coastal-band, yellow, and NIR-II compared to those of bare soil pixels (Figure 22c). These pixels are divided into nonbare soil, which reduced the integrity of the bare soil in the classification result based on data 1. The spectral values of these vegetation pixels In Red-edge, $PTI_{Red\text{-}edge}$, $PTI_{NIR\text{-}II}$, and $PTI_{Coastal\text{-}band}$ are very close to that of bare soil (Figure 22c). Therefore, most of the vegetation pixels covering bare soil were classified as bare soil, and the integrity of the bare soil was significantly improved in the classification result based on data 2.

Based on the analysis and discussion of the classification results based on two sets of data about two experimental areas, we conclude that PTI images contain texture and edge features that are completely different from spectral features. Combining such image data can expand the classification feature space's dimension and improve the classification accuracy.

Analysis of Segmental Results

To ensure the rationality of evaluation, we visually compared and quantitatively evaluated and analyzed the segmental results in two experimental areas.

Visual Comparison

Visually comparing the segmentation results of the first experimental area based on the two data sets reveals the following: (1) For the segmentation results based on data 1 (Figure 20a), due to the spectral heterogeneity within the same land-cover type, the buildings in white boxes ①, ②, ③, and ④ are oversegmented into many small objects, i.e., "oversegmentation," and the boundaries of these polygons do not correspond to the actual edges of the buildings. However, in the white boxes of the segmentation results based on data 2 (Figure 20b), the oversegmentation phenomenon disappears. In addition, the contour lines of the objects are nearly consistent with the actual edges of buildings. (2) For the segmentation results based on data 1 (Figure 20a), due to the spectral heterogeneity within the same land-cover type, the shadow of the building in white boxes ①, ②, ③, and ④ is oversegmented. On the other hand, the shadow is segmented more accurately in the results of data 2 (Figure 20b). (3) During segmentation, spectral heterogeneity causes the vegetation in white boxes ⑤ and ⑥ to be oversegmented when considering data 1 (Figure 20a), while the segmentation integrity of vegetation improves when considering data 2 (Figure 20b).

Subsequently, visually comparing the segmentation results of the second experimental area based on the two sets of data reveals: (1) For the segmentation result based on data 1 (Figure 20c), due to the

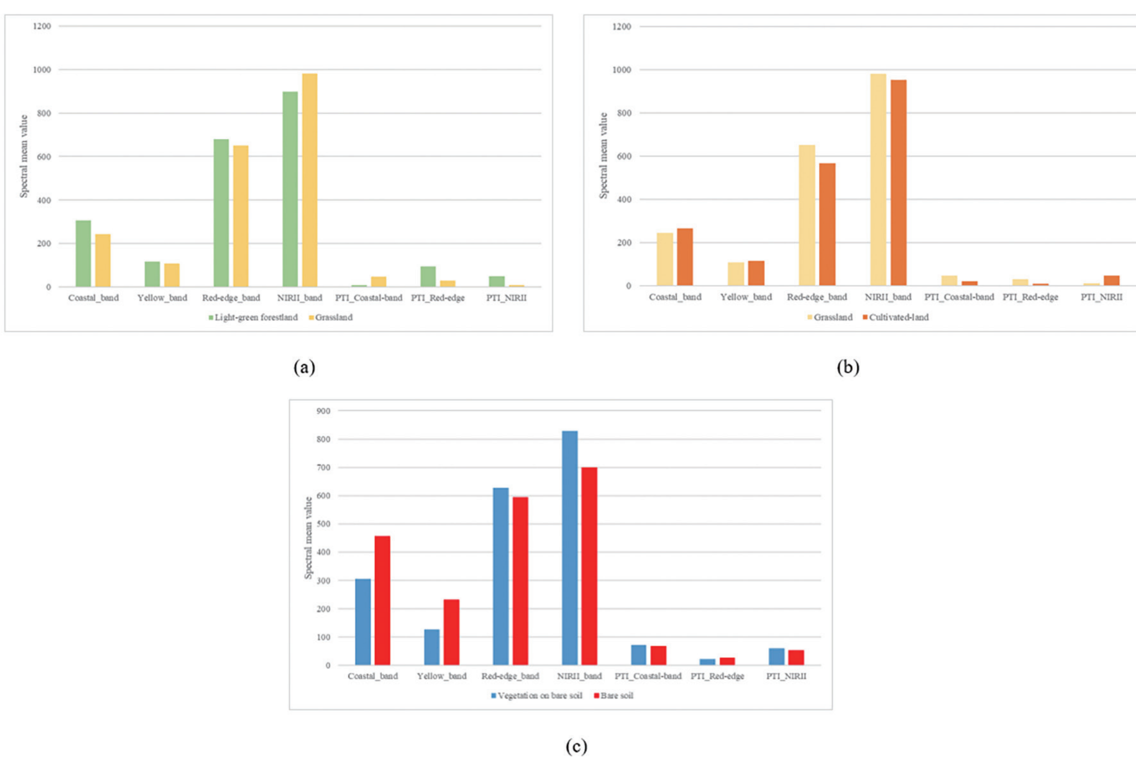

Figure 22. Comparison of the spectral mean values of some pixels in the second experimental area about multi-spectral images. (a) Light-green forestland pixels versus grassland pixels. (b) Grassland pixels versus cultivated-land pixels. (c) Vegetation on bare soil pixels versus bare soil pixels. NIRII = near-infrared II; PTI = pixel texture index.

spectral heterogeneity within the same land-cover type, the woodland in white box ① is oversegmented into multiple objects, while the woodland in the segmental result based on data 2 (Figure 20d) is completely segmented. (2) In the segmentation results based on data 1 (Figure 20c), due to the spectral heterogeneity within the same land-cover type and of different land-cover types, the farmland in white box ② suffers from oversegmentation and undersegmentation. However, these phenomena disappear in the white box of the segmental result based on data 2 (Figure 20d). (3) For the segmentation results based on data 1 (Figure 20c), due to the spectral heterogeneity, bare soil in white box ③ is oversegmented, while in the segmentation results based on data 2 (Figure 20d), the oversegmentation problem was significantly improved. (4) Some edges of terraces in white box ④ are not displayed in the segmental result based on data 1 (Figure 20c), but they are shown in the segmental results based on data 2 (Figure 20d).

Quantitative Evaluation of Segmental Results

Opposing the unsuitable image classification evaluation indicators, i.e., overall accuracy and kappa coefficient, this article uses five supervised evaluative indicators: oversegmentation (OS), undersegmentation (US), edge matching degree (ED), number of segmentation blocks (FG), and shape error (SH), which evaluate the difference between the segmentation result and the ground truth segmentation to evaluate the segmentation quality quantitatively (Wu *et al.* 2013; Chen *et al.* 2017). All metrics have a range of [0, 1], and their values are inversely proportional to the difference between the segmentation result and the ground truth segmentation. The evaluation is conducted as follows: Based on the PAN image, the corrected segmental results for the two experimental areas are obtained by a manual drawing (Figures 23a and 24a). Then, according to the distributed proportion of each land-cover type, sample objects are randomly selected from different image regions. The sampling results are presented in Figures 23b, 23c, 24b, and 24c, and the sample objects are outlined in red. Eventually, the five evaluative indicators estimate the difference between sample objects and their respective ground truth segmentation (Table 5).

Table 5. Quantitative evaluation about segmental results of both experimental areas.

Segmental Results	Supervised Evaluative Indicators				
	OS	US	ED	FG	SH
Segmental result based on data 1 of the first experimental area	0.1494	0.0088	0.6469	0.8565	0.0779
Segmental result based on data 2 of the first experimental area	0.0623	0.0047	0.3801	0.2135	0.0416
Segmental result based on data 1 of the second experimental area	0.7379	0.1282	0.9477	0.9519	0.0896
Segmental result based on data 2 of the second experimental area	0.3256	0.0773	0.5782	0.518	0.0648

ED = edge-matching degree; FG = number of segmentation blocks; OS = oversegmentation; SH = shape error; US = undersegmentation.

Analysis and Evaluation of Segmental Results

The values of five evaluation indicators (Wu *et al.* 2013) reveal the following: (1) Compared to the values of OS and US in data 1, the decline rates of OS and US values of the segmentation result based on data 2 about the first experimental area are 58.2% and 46.5%, respectively. The decline rates of OS and US values of the segmentation result based on data 2 about the second experimental area are 55.8% and 39.7%. The large decline rates of OS and US values about the segmentation results based on data 2 indicate that the oversegmentation and undersegmentation phenomena are effectively reduced by combining PTI and PAN images during segmentation. (2) Compared to the values of ED, FG, and SH for data 1, the decline rates of ED, FG, and SH values of the segmentation result based on data 2 about the first experimental area are 41.2%, 75%, and 46.5%. The decline rates of ED, FG, and SH values of the segmentation result based on data 2 about the second experimental area are 38.9%, 45.5%, and 27.6%. The decline rates of ED, FG, and SH values about the segmentation results based on data 2 indicate that

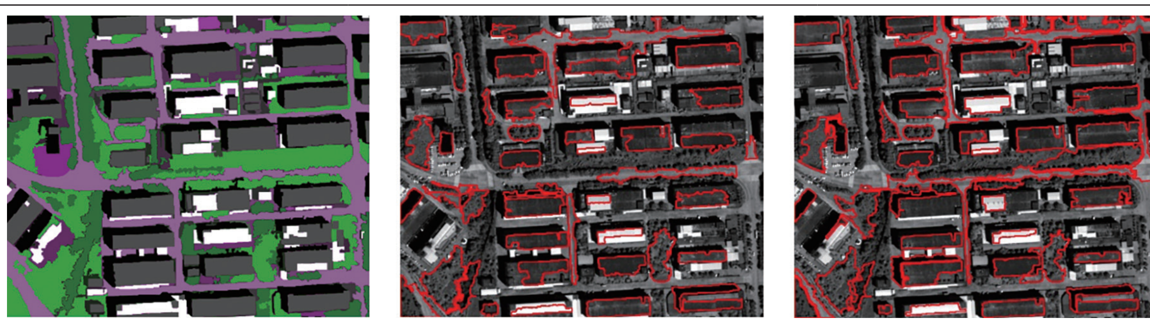

(a) (b) (c)

Figure 23. Manually corrected segmental results and sample objects of the first experimental area about PAN image. (a) Manually corrected segmental result; (b) Sample objects of the segmental results based on data 1. (c) Sample objects of the segmental result based on data 2.

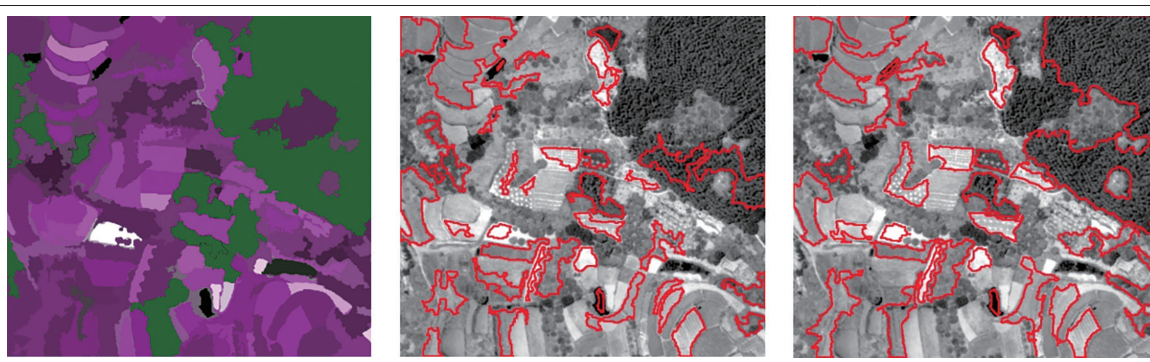

(a) (b) (c)

Figure 24. Manually corrected segmental results and sample objects of the second experimental area about PAN images. (a) Manually corrected segmental result. (b) Sample objects of the segmental results based on data 1. (c) Sample objects of the segmental results based on data 2.

the segmentation results based on data 2 are more similar to the ground truth segmentation than the segmentation result based on data 1.

Furthermore, the high-quality segmentation results based on data 2 indicate that PTI is a good texture descriptor. Indeed, it improves the homogeneity of texture features within the same land-cover type by using the context of the intrapixel texture features and ultimately highlighting the edges of the land-cover types. Meanwhile, the PTI image is obtained based on the LTBC image using the PTI algorithm (see "Calculation of PTI"), which can mitigate the effect of different illumination on PTI image data. Overall, we conclude that combining PTI and PAN images eliminates the interference of high-frequency information during the segmentation process and introduces texture and edge features to improve the segmentation quality.

Conclusions

This article proposes a PTI and its corresponding algorithm that mitigates the interference of different illumination to the analytical process of texture features without placing constraints regarding texture regularity. The experiments on three types of HSRRS images (i.e., IKONOS, QuickBird, and WorldView-II) prove that PTI simultaneously enhances the homogeneity of texture features within the same land-cover type and the edge features of different land-cover types. Combining this image data can expand the classification feature space's dimension and improve the classification accuracy and quality. Indeed, accuracy improved from 7% to 14%, and the kappa increased from 11% to 24%. Additionally, the experiments prove that combining such features for image segmentation effectively reduces the oversegmentation and undersegmentation phenomena. Five supervised evaluative indicators are reduced from 27.6% to 75%.

Acknowledgments

This work was supported by Science and Technology Project of Fuzhou Polytechnic with Project FZYKJJJYB202101.

References

Abdullah, M.F.A., M. S. Sayeed, K. S. Muthu, H. K. Bashier, A. Azman and S. Z. Ibrahim. 2014. Face recognition with symmetric local graph structure (SLGS). *Expert Systems with Applications* 41(14):6131–6137.

Alata, O. and C. Olivier. 2003. Choice of a 2-D causal autoregressive texture model using information criteria. *Pattern Recognition Letters* 24(9–10):1191–1201.

Andrearczyk, V. and P. F. Whelan. 2016. Using filter banks in convolutional neural networks for texture classification. *Pattern Recognition Letters* 84:63–69.

Arivazhagan, S. and L. Ganesan. 2003. Texture classification using wavelet transform. *Pattern Recognition Letters* 24(9–10):1513–1521.

Arivazhagan, S., L. Ganesan and S. P. Priyal. 2006. Texture classification using Gabor wavelets based rotation invariant features. *Pattern Recognition Letters* 27(16):1976–1982.

Arvor, D., L. Durieux, S. Andrés and M.-A. Laporte. 2013. Advances in geographic object-based image analysis with ontologies: A review of main contributions and limitations from a remote sensing perspective. *ISPRS Journal of Photogrammetry and Remote Sensing* 82:125–137.

Backes, A. R., W. N. Gonçalves, A. S. Martinez and O. M. Bruno. 2010. Texture analysis and classification using deterministic tourist walk. *Pattern Recognition* 43(3):685–694.

Balaguer, A., L. Ruiz, T. Hermosilla and J. A. Recio. 2010. Definition of a comprehensive set of texture semivariogram features and their evaluation for object-oriented image classification, *Computers & Geosciences* 36(2):231–240.

Blaschke, T., G. J. Hay, M. Kelly, S. Lang, P. Hofmann, E. Addink, R. Q. Feitosa, F. Van der Meer, H. Van der Werff and F. Van Coillie. 2014. Geographic object-based image analysis–towards a new paradigm. *ISPRS Journal of Photogrammetry and Remote Sensing* 87:180–191.

Brochard, J., M. Khoudeir and B. Augereau. 2001. Invariant feature extraction for 3D texture analysis using the autocorrelation function. *Pattern Recognition Letters* 22(6–7):759–768.

Chen, Y., D. Ming, L. Xu and L. Zhao. 2017. An overview of quantitative experimental methods for segmentation evaluation of high spatial remote sensing images. *Journal of Geo-Information Science* 19(6):818–830.

Corcoran, P., A. Winstanley and P. Mooney. 2010. Segmentation performance evaluation for object-based remotely sensed image analysis. *International Journal of Remote Sensing* 31(3):617–645.

Dai, Q., B. Luo, C. Zheng and L. Wang. 2020. Regional multiscale Markov random field for remote sensing image classification. J, *Remote Sensing (Chinese)* 24(3):245–253.

Decenciere, E., B. Marcotegui and F. Meyer. 2001. Content-dependent image sampling using mathematical morphology: Application to texture mapping. *Signal Processing: Image Communication* 16(6):567–584.

Duan, Y., F. Liu, L. Jiao, P. Zhao and L. Zhang. 2017. SAR image segmentation based on convolutional-wavelet neural network and Markov random field. *Pattern Recognition* 64:255–267.

Espinosa, R., R. Bailón and P. Laguna. 2021. Two-dimensional EspEn: A new approach to analyze image texture by irregularity. *Entropy* 23(10):1261.

Feng, X., J. Zhang and J. Tang. 2021. Depth extraction method of remote sensing image elements for spatiotemporal distribution of water pollution. *Computer Simulation* 38(6):121–124+178.

He, Y. and K. Changqing. 2011. Application of semivariogram texture distilling for remote sensing image classification. *Remote Sensing Technology and Application* 23(5):571–575.

Hu, Z., G. Liu and Y. Su. 2018. Application of local autocorrelation function in content-based image retrieval. *Computer Science* 45(11A):259–262.

Lin, W., Y. Li and Q. Zhao. 2019. High-resolution remote sensing image segmentation using minimum spanning tree tessellation and RHMRF-FCM algorithm. *Acta Geodaetica et Cartographica Sinica* 48(1):64.

Lin, H.-C., L.-L. Wang and S.-N. Yang. 1997. Extracting periodicity of a regular texture based on autocorrelation functions. *Pattern Recognition Letters* 18(5):433–443.

Liu, L., S. Lao, P. W. Fieguth, Y. Guo, X. Wang and M. Pietikäinen. 2016. Median robust extended local binary pattern for texture classification. *IEEE Transactions on Image Processing* 25(3):1368–1381.

Liu, R., X. Ma, X. Lu, M. Wang and P. Wang. 2022. Automatic extraction of urban road boundaries using diverse LBP features. *National Remote Sensing Bulletin* 26(3):541–554.

Liu, H., W. Ren, R. Wang and X. Cao. 2022. A super-resolution transformer fusion network for single blurred image. *Journal of Image and Graphics* 27(5):1616–1631.

Liu, H., H. Wei, L. Wei, J. Li and Z. Yang. 2015. An experiment on wear particle's texture analysis and identification by using deterministic tourist walk algorithm. *Industrial Lubrication and Tribology* 67(6):582–593.

Lu, S.-Y. and K. S. Fu. 1978. A syntactic approach to texture analysis. *Computer Graphics and Image Processing* 7(3):303–330.

Padhy, R., A. Dash, S. K. Dash and J. Mishra. 2021. Improved face recognition with fractal-based texture analysis. *International Journal of Computer Vision and Image Processing* 11(3):41–53.

Palm, C. 2004. Color texture classification by integrative co-occurrence matrices. *Pattern Recognition* 37(5):965–976.

Pun, C.-M. and H.-M. Zhu. 2009. Textural image segmentation using discrete cosine transform. *Proceedings of the 3rd International Conference on Communications and Information Technology*, pp. 54–58. (Vouliagmeni Athens Greece December 29 - 31, 2009.)

Qian, X., X.-S. Hua, P. Chen and L. Ke. 2011. PLBP: An effective local binary patterns texture descriptor with pyramid representation. *Pattern Recognition* 44(10–11):2502–2515.

Qian, Y., M. Ye and J. Zhou. 2012. Hyperspectral image classification based on structured sparse logistic regression and three-dimensional wavelet texture features. *IEEE Transactions on Geoscience and Remote Sensing* 51(4):2276–2291.

Rebhi, A., S. Abid and F. Fnaeich. 2019. Texture defect detection using local homogeneity and discrete cosine transform. *World Applied Sciences Journal* 31(9):1677–1683.

Samiappan, S., G. Turnage, L. Hathcock, L. Casagrande, P. Stinson and R. Moorhead. 2017. Using unmanned aerial vehicles for high-resolution remote sensing to map invasive *Phragmites australis* in coastal wetlands. *International Journal of Remote Sensing* 38(8–10):2199–2217.

Sayeed, S., I. Yusof, H. K. Bashier, J. Hossen and M. Azli. 2013. Plant identification based on leaf shape and texture pattern using local graph structure (LGS). *Australian Journal of Basic and Applied Sciences* 7(11):29–35.

Silva, L. E., J. J. Duque, J. C. Felipe, L. O. Murta Jr and A. Humeau-Heurtier. 2018. Two-dimensional multiscale entropy analysis: Applications to image texture evaluation. *Signal Processing* 147:224–232.

Teillet, C., B. Pillot, T. Catry, L. Demagistri, D. Lyszczarz, M. Lang, P. Couteron, N. Barbier, A. Adou Kouassi and Q. Gunther. 2021. Fast unsupervised multiscale characterization of urban landscapes based on earth observation data. *Remote Sensing* 13(12):2398.

Wu, B., S. Lin and G. Zhou. 2013. Quantitatively evaluating indexes for object-based segmentation of high spatial resolution image. *Journal of Geo-information Science* 4(15):567–573.

Wu, X., J. Peng, J. Shan and W. Cui. 2015. Evaluation of semivariogram features for object-based image classification., *Geo-spatial Information Science* 18(4):159–170.

Zhang, X. and T. Li. 2022. Breast cancer pathological image classification based on cycle-GAN and improved DPN network. *Journal of Zhejiang University (Engineering Science)* 56(4):727–735.

Zhang, Z., J. Li and Z. Shen. 2006. Analysis on texture discrimination performance of moments of local Fourier transform coefficients. *Journal of Image and Graphics* 11(1):33–40.

Zhang, T., B. Mei, L. Qiao, H. Yang and W. Zhu. 2020. Detection method for composite hole guided by texture boundary. *Journal of Zhejiang University (Engineering Science)* 54(12):2294–2300.

Zhang, D., X. Zhang, L. Li and H. Liu. 2022. Remote sensing image segmentation based on Parzen window density estimation of super-pixels. *Remote Sensing for Natural Resources* 34(1):53–60.

Zunino, L. and H. V. Ribeiro. 2016. Discriminating image textures with the multiscale two-dimensional complexity-entropy causality plane. *Chaos, Solitons & Fractals* 91:679–688.

In-Press Articles

Haotian Zheng, Fan Yu, Huawei Wan, Peirong Shi, and Haonan Wang. Land Use Change in the Yangtze River Economic Belt during 2010 to 2020 and Future Comprehensive Prediction Based on Markov and ARIMA Models.

Fangrong Zhou, Lifeng Liu, Hao Hu, Weishi Jin, Zezhong Zheng, Zhongnian Li, Yi Ma, and Qun Wang. An Improved YOLO Network for Insulator and Insulator Defect Detection in UAV Images.

Yinsheng Zhang, Ru Ji, Yuxiang Hu, Yulong Yang, Xin Chen, Xiuxian Duan, and Huilin Shan. Real-Time Semantic Segmentation of Remote Sensing Images for Land Management.

Stephanie A. Insalaco, Hannah V. Herrero, Russ Limber, Clancy Oliver, and William B. Wolfson. Monitoring an Ecosystem in Crisis: Measuring Seagrass Meadow Loss Using Deep Learning in Mosquito Lagoon, Florida.

Parcel-Level Crop Classification in Plain Fragmented Regions Based on Multi-Source Remote Sensing Images

Qiao Zhang, Ziyi Luo, Yang Shen, and Zhoufeng Wang

Abstract

Accurately obtaining crop cultivation extent and estimating the cultivated area are significant for adjusting regional planting structure. This study proposes a parcel-level crop classification method using time-series, medium-resolution, remote sensing images and single-phase, high-spatial-resolution, remote sensing images. The deep learning semantic segmentation network feature pyramid network with squeeze-and-excitation network (FPN–SENet) and multi-scale segmentation were used to extract cultivated land parcels from Gaofen-2 imagery, while the pixel-level crop types were classified by using support vector machine algorithms from time-series Sentinel-2 images. Then, the parcel-level crop classification was obtained from the pixel-level crop types and land parcels. The proposed method was tested in southwestern China to extract main winter–spring crops and achieved a good performance. Specifically, the FPN-SENet model outperformed other models in cultivated land extraction, with an F1 of 0.872. The crop classification overall accuracy is 0.910 and the kappa coefficient is 0.861. This study provides a technical reference for monitoring cultivated land and can be applied in other regions.

Introduction

By 2050, the worsening soil, land, and water resources on a global scale will present a huge challenge in meeting the food demands of over 10 billion people (United Nations 2017; Food and Agriculture Organization of the United Nations FAO 2021). Food security is a pressing global concern, and the strictest protection policies should be implemented on cultivated land, the basis of food production. Therefore, accurately monitoring cultivated land is significant for adjusting regional planting structure, improving management of crops, and ensuring food security (Yan *et al.* 2015). As a new earth observation technology, remote sensing has the characteristics of excellent efficiency, wide range, and high accuracy. In recent years, with the continuous development of remote sensing technology, ground object identification based on remote sensing has gradually replaced the traditional manual field investigation and has been widely used in agriculture, such as crop classification and monitoring regional planting structure (Yan *et al.* 2015; Kong *et al.* 2016).

With the increase in available remote sensing images, such as those from Moderate Resolution Imaging Spectroradiometer (MODIS), Landsat, and Sentinel, it is found that a single-phase image cannot be universally applied in precise crop classification due to the limitations of resolution, cloud, and rain. Meanwhile, multi-temporal images are found to be able to achieve higher classification accuracy (Yang *et al.* 2019; Li *et al.* 2021). Since the multi-temporal images contain an enormous amount of vegetation phenological information, these images can show the unique phenological characteristics of the crops during the growth cycle (Xie *et al.* 2008; Chen and Liu 2023). Therefore, time-series images are widely used in current research (Zheng *et al.* 2015), among which the time-series medium-to-high resolution images are the main data source in mapping crops now (Du *et al.* 2019). Several methods like maximum likelihood (ML) (Ha *et al.* 2020), support vector machine (SVM) (Foody and Mathur 2004), random forest (RF) (Breiman 2001), and classification and regression tree (CART) (Loh 2011) were proposed for crop classification using time-series medium-to-high resolution images (Belgiu and Csilik 2018; Zhang *et al.* 2020).

However, due to the complex land cover situation, the accuracy of crop mapping is not very high with only phenological characteristics from time-series images during its growth cycle, especially in highly heterogeneous cultivated land and broken areas (Wu *et al.* 2017). For example, some regions, such as the Chengdu Plain in the Southwest of China, are mainly smallholder agriculture (Du *et al.* 2019), with fragmented cultivated land parcels and complex planting structures. If crops were mapped by time series medium-resolution images, there are 3 main challenges: over-or-under estimate of the crop areas caused by obvious mixed pixels at the edge of cultivated lands (Wu *et al.* 2017; Wen *et al.* 2023), a noticeable salt-and-pepper effect (Blaschke *et al.* 2000) caused by crops at various growing stages and the spatial heterogeneity (Chen and Liu 2023), and misidentified crop classification due to the similar phenological characteristics in areas with complex planting structure. These challenges make it difficult to meet practical needs with the mapping results. To address these problems, a good solution is to introduce the parcel edges as boundary constraints for the pixel-level crop classification.

High-spatial-resolution images can provide the necessary details to observe smallholder agriculture (Du *et al.* 2019), and some scholars have extracted cultivated land boundaries and parcels from such images (Xu *et al.* 2022). Yao *et al.* (2014) used the traditional object-based image classification (OBIC) method to extract the cultivated land from the RapidEye images. They also found that the segmentation technique can obtain objects with similar spectral-spatial characteristics, and the segmentation scheme determines the accuracy of classification results.

With the development of deep learning, it can extract cultivated land boundaries with high precision (Liu *et al.* 2022). Deep learning is a self-supervised feature learning method that simulates and learns how the human brain thinks by constructing neural networks (Hinton *et al.* 2006). Unlike other traditional classifiers, it can learn a deep nonlinear network structure, approximate complex functions to extract

Qiao Zhang is with the School of Geoscience and Technology, Southwest Petroleum University(swpuqzh@swpu.edu.cn).

Ziyi Luo is with the School of Geoscience and Technology, Southwest Petroleum University.

Yang Shen is with the Third Geodetic Surveying Brigade of Ministry of Natural Resources.

Zhoufeng Wang is with the School of Geoscience and Technology, Southwest Petroleum University.

Corresponding author: Qiao Zhang (swpuqzh@swpu.edu.cn)

Contributed by Dongdong Wang, June 28, 2023 (sent for review December 2, 2023; reviewed by Jinlong Fan, Weijia Chen, Zhan Zhao).

Photogrammetric Engineering & Remote Sensing
Vol. 90, No. 5, May 2024, pp. 293–302.
0099-1112/22/293–302

doi: 10.14358/PERS.23-00053R2

PEER-REVIEWED CONTENT
IS ONLY AVAILABLE TO
ASPRS MEMBERS AND SUBSCRIBERS

FOR MORE INFORMATION VISIT
MY.ASPRS.ORG

PEER-REVIEWED CONTENT
IS ONLY AVAILABLE TO
ASPRS MEMBERS AND SUBSCRIBERS

FOR MORE INFORMATION VISIT
MY.ASPRS.ORG

PEER-REVIEWED CONTENT
IS ONLY AVAILABLE TO
ASPRS MEMBERS AND SUBSCRIBERS

FOR MORE INFORMATION VISIT
MY.ASPRS.ORG

**PEER-REVIEWED CONTENT
IS ONLY AVAILABLE TO
ASPRS MEMBERS AND SUBSCRIBERS**

**FOR MORE INFORMATION VISIT
MY.ASPRS.ORG**

**PEER-REVIEWED CONTENT
IS ONLY AVAILABLE TO
ASPRS MEMBERS AND SUBSCRIBERS**

**FOR MORE INFORMATION VISIT
MY.ASPRS.ORG**

PEER-REVIEWED CONTENT IS ONLY AVAILABLE TO ASPRS MEMBERS AND SUBSCRIBERS

FOR MORE INFORMATION VISIT MY.ASPRS.ORG

**PEER-REVIEWED CONTENT
IS ONLY AVAILABLE TO
ASPRS MEMBERS AND SUBSCRIBERS**

**FOR MORE INFORMATION VISIT
MY.ASPRS.ORG**

PEER-REVIEWED CONTENT
IS ONLY AVAILABLE TO
ASPRS MEMBERS AND SUBSCRIBERS

FOR MORE INFORMATION VISIT
MY.ASPRS.ORG

Evaluation of SMAP and CYGNSS Soil Moistures in Drought Prediction Using Multiple Linear Regression and GLDAS Product

Komi Edokossi, Shuanggen Jin, Andres Calabia, Iñigo Molina, and Usman Mazhar

Abstract

Drought is a devastating natural hazard and exerts profound effects on both the environment and society. Predicting drought occurrences is significant in aiding decision-making and implementing effective mitigation strategies. In regions characterized by limited data availability, such as Southern Africa, the use of satellite remote sensing data promises an excellent opportunity for achieving this predictive goal. In this study, we assess the effectiveness of Soil Moisture Active Passive (SMAP) and Cyclone Global Navigation Satellite System (CYGNSS) soil moisture data in predicting drought conditions using multiple linear regression–predicted data and Global Land Data Assimilation System (GLDAS) soil moisture data. SMAP and CYGNSS data exhibit strong spatiotemporal congruence with the predicted soil moisture data. Pearson correlation coefficients further underscore this consistency, with correlations of r = 0.78 between GLDAS and SMAP, r = 0.61 between GLDAS and CYGNSS, and r = 0.84 between GLDAS and the estimated soil moisture. The proficient performance of SMAP and CYGNSS soil moisture data in tandem with other variables underscores their efficacy in predicting drought conditions.

Introduction

Drought constitutes a significant natural hazard characterized by prolonged periods of low precipitation and elevated temperatures, leading to heightened evapotranspiration rates (Jin and Zhang 2016; Huang and Jin 2020; Elameen *et al.* 2023). This climatic phenomenon directly impacts agricultural yields due to deficits in soil moisture (Marsh, 2007; Dai 2011). Within the context of the Southern Africa region, the effect of recent drought events, spanning from 2015–2016 to 2018–2020, has been particularly profound. These occurrences have exacted a heavy toll on both human livelihoods and crop yields. For instance, during the drought of 2015–2016, crop production underwent a precipitous decline of up to 66%, concurrently affecting over a quarter of the region's population (Ainembabazi, 2018). During 2018–2019, the drought affected more than 40% of the population (Johannesburg Regional Bureau 2020), and the crop production was 10% below the average (World Food Program 2019).

The scientific literature commonly recognizes four distinct categories of drought (Mishra and Singh 2010): meteorological, agricultural, hydrological, and socioeconomic. Meteorological drought manifests as an insufficient occurrence of precipitation over a given time span—whether short or prolonged—resulting in a deficit of soil moisture that adversely affects plants, giving rise to what is termed agricultural drought. Hydrological drought materializes when there is an insufficiency in water availability across streams, reservoirs, and groundwater sources. In contrast, socioeconomic drought pertains to the inability of water supply to adequately meet demand (Mishra and Singh 2010).

The prediction of drought occurrences plays a pivotal role in facilitating early warnings and mitigating their subsequent effects. Over time, numerous methodologies and formulations have been developed and used to achieve this objective. The predominant approaches comprise statistical methods and dynamical methods, which harness climate and/or hydrologic models to simulate the intricate physical processes of the atmosphere, land, and oceans (Hao *et al.* 2018). Within the realm of statistical methods, a spectrum of techniques is embraced, including time series models, regression models, artificial intelligence models, Markov chain models, and conditional probability models. These methodologies stand out as extensively used avenues. In the context of statistical methodologies, the identification of appropriate predictors derived from atmospheric, terrestrial, and oceanic domains, as well as the determination of predictands for the target timeframe, is of paramount importance (Hao *et al.* 2018). For instance, the efficacy of time series models predominantly hinges on the persistence of certain indicators, which serves as the bedrock for achieving accurate predictions. The autoregressive integrated moving average technique emerges as an exceptionally apt choice for prediction within climatology and hydrology, as it effectively handles linear relationships between predictors and predictands, albeit without capturing nonlinearity. In the realm of statistical prediction, the conventional linear regression method finds applications in hydrology and climatology. This method establishes a linear connection between the predictand and suitable predictors, representing the simplest avenue for climatohydrological prediction. The modeling of the association between drought indices and predictors often uses the regression model (Barros and Bowden 2008; Liu and Juárez 2001; Panu and Sharma 2002; Sun *et al.* 2012). In scenarios in which nonlinear relationships are at play, the locally weighted polynomial regression offers a valuable alternative for modeling associations (Hwang and Carbone 2009; Liu and Hwang

Komi Edokossi is with the School of Remote Sensing and Geomatics Engineering, Nanjing University of Information Science and Technology, Nanjing 210044, China.

Shuanggen Jin is with the School of Remote Sensing and Geomatics Engineering, Nanjing University of Information Science and Technology, Nanjing 210044, China; the Shanghai Astronomical Observatory, Chinese Academy of Sciences, Nanjing 210044, China; and the School of Surveying and Land Information Engineering, Henan Polytechnic University, Nanjing 210044 (sgjin@nuist.edu.cn).

Andres Calabia is with the Department of Physics and Mathematics, University of Acala, Nanjing 210044.

Iñigo Molina is with the School of Remote Sensing and Geomatics Engineering, Nanjing University of Information Science and Technology, Nanjing 210044; and the School of Land Surveying, Geodesy and Mapping Engineering, Universidad Politécnica de Madrid, Nanjing 210044.

Usman Mazhar is with the School of Remote Sensing and Geomatics Engineering, Nanjing University of Information Science and Technology, Nanjing 210044.

Corresponding author: Shuanggen Jin (sgjin@nuist.edu.cn)

Contributed by Prasad S. Thenkabail, October 13, 2023 (sent for review November 8, 2023; reviewed by Itiya Aneece, Xiaodong Li, Xutong Niu).

Photogrammetric Engineering & Remote Sensing
Vol. 90, No. 5, May 2024, pp. 303–312.
0099-1112/22/303–312

doi: 10.14358/PERS.23-00075R2

PEER-REVIEWED CONTENT
IS ONLY AVAILABLE TO
ASPRS MEMBERS AND SUBSCRIBERS

FOR MORE INFORMATION VISIT
MY.ASPRS.ORG

**PEER-REVIEWED CONTENT
IS ONLY AVAILABLE TO
ASPRS MEMBERS AND SUBSCRIBERS**

**FOR MORE INFORMATION VISIT
MY.ASPRS.ORG**

PEER-REVIEWED CONTENT
IS ONLY AVAILABLE TO
ASPRS MEMBERS AND SUBSCRIBERS

FOR MORE INFORMATION VISIT
MY.ASPRS.ORG

PEER-REVIEWED CONTENT
IS ONLY AVAILABLE TO
ASPRS MEMBERS AND SUBSCRIBERS

FOR MORE INFORMATION VISIT
MY.ASPRS.ORG

PEER-REVIEWED CONTENT
IS ONLY AVAILABLE TO
ASPRS MEMBERS AND SUBSCRIBERS

FOR MORE INFORMATION VISIT
MY.ASPRS.ORG

PEER-REVIEWED CONTENT
IS ONLY AVAILABLE TO
ASPRS MEMBERS AND SUBSCRIBERS

FOR MORE INFORMATION VISIT
MY.ASPRS.ORG

PEER-REVIEWED CONTENT
IS ONLY AVAILABLE TO
ASPRS MEMBERS AND SUBSCRIBERS

FOR MORE INFORMATION VISIT
MY.ASPRS.ORG

PEER-REVIEWED CONTENT
IS ONLY AVAILABLE TO
ASPRS MEMBERS AND SUBSCRIBERS

FOR MORE INFORMATION VISIT
MY.ASPRS.ORG

Debris Flow Susceptibility Evaluation Based on Multi-level Feature Extraction CNN Model: A Case Study of Nujiang Prefecture, China

Xu Wang, Baoyun Wang, Ruohao Yuan, Yumeng Luo, and Cunxi Liu

Abstract

Debris flow susceptibility evaluation plays a crucial role in the prevention and control of debris flow disasters. Therefore, this paper proposes a convolutional neural network model named multi-level feature extraction network (MFENet). First, a dual-channel CNN architecture incorporating the Embedding Channel Attention mechanism is used to extract shallow features from both digital elevation model images and multispectral images. Subsequently, channel shuffle and feature concatenation are applied to the features from the two channels to obtain fused feature sets. Following this, a deep feature extraction is performed on the fused feature sets using a residual module improved by maximum pooling. Finally, the susceptibility index of gullies to debris flows is calculated based on the similarity scores. Experimental results demonstrate that the model exhibits favorable classification performance, with an accuracy of 73.45%. Furthermore, the percentage of debris flow valleys in high and very high susceptibility zones reaches 93.97%.

Introduction

Debris flows refer to a specific type of flood event characterized by the rapid transport of a significant amount of solid materials, such as mud, sand, rocks, and large boulders, triggered by heavy precipitation in mountain valleys or slopes. Debris flows are characterized by their sudden onset, high velocity, large discharge, substantial material capacity, and destructive potential. Incidents of debris flows often result in the destruction of transportation infrastructure, including roads and railways, as well as residential areas, leading to significant losses (Lopes *et al.* 2016). This prompts many researchers to evaluate debris flow susceptibility, aiming to prevent and control disasters (Musumeci *et al.* 2021).

Since the 1970s, the evaluation of debris flow susceptibility has gradually become an important research direction for disaster prevention and mitigation. The former Soviet Union published a national zoning map for debris flow-prone regions (Fleischmann 1985). Japanese experts determined debris flow susceptibility based on three aspects: landforms, morphology of debris flow, and rainfall (Li 1997; Takahashi 1991). Chinese researchers (Liu 1991) divided ten counties and cities in Zhaotong City, Yunnan Province, into four levels of hazard zones using a regional debris flow hazard determination method. During this stage of debris flow research, qualitative evaluation was the main approach, relying heavily on expert experience and field investigations, which were time-consuming, labor-intensive, inefficient, and carried certain risks. With the rapid development of remote sensing, geographic information systems, and global positioning systems (referred to as "3S" technologies) in the late 1990s, these technologies began to be applied in the investigation and monitoring of debris flows, promoting the development of quantitative evaluation in geological disaster research. Researchers started using 3S technologies and statistical methods for debris flow susceptibility evaluation (Zhang *et al.* 2019; Jamali *et al.* 2020; Li *et al.* 2022). Li (2019) used remote sensing imagery as data sources and selected the certainly factor model (CF) and CF-based multi-factor overlay weight method for debris flow susceptibility evaluation. Li *et al.* (2019) also used remote sensing and geographic information technologies, combined with three-dimensional visualization techniques, to extract debris flow information. They selected nine evaluation factors and used an improved analytic hierarchy process for susceptibility evaluation.

With the popularity of machine learning, researchers have found that it can capture the nonlinear relationship between debris flow susceptibility and evaluation factors more accurately. Various machine learning algorithms have been widely applied in debris flow susceptibility evaluation. Wang (2018), Liu and Qiao (2021), and Li *et al.* (2010) have established debris flow susceptibility models based on support vector machines. Wang Xin *et al.* (2022) used correlation analysis to select influential factor indicators and constructed a dynamic zoning model for debris flow susceptibility using a back propagation neural network. Liu *et al.* (2018) built a debris flow susceptibility evaluation model by random forests. Machine learning algorithms have shown good performance in debris flow susceptibility evaluation. However, they require subjective selection of susceptibility factors through correlation analysis or other methods and involve significant human intervention, resulting in a lower degree of classification automation. Convolutional neural networks (CNNs) have significant advantages in image classification and other fields, avoiding the process of selecting susceptibility evaluation factors and simplifying the complexity of feature extraction and data reconstruction in the classification process. Che (2021) proposed a debris flow susceptibility evaluation method based on a CNN model, demonstrating the superiority of the model. Zhang (2021) established a multi-sequence residual network model based on the attention mechanism to predict debris flow velocity, demonstrating the coupling correlation between velocity and various triggering factors, with slope and bulk density significantly affecting velocity. However, there are still some issues to be addressed. Debris flow is a type of geological hazard in valleys, and it is crucial to construct a CNN model that can adequately represent the spatial

Xu Wang is with the School of Mathematics, Yunnan Normal University.

Baoyun Wang is with the School of Mathematics and the Key Laboratory of Modern Analytical Mathematics and Applications, Yunnan Normal University.

Ruohao Yuan is with the School of Mathematics, Yunnan Normal University.

Yumeng Luo is with the School of Mathematics, Yunnan Normal University.

Cunxi Liu is with the School of Mathematics, Yunnan Normal University.

Corresponding author: Baoyun Wang (wspbmly@163.com)

Contributed by Prasad S. Thenkabail, October 13, 2023 (sent for review November 8, 2023; reviewed by Itiya Aneece, Xiaodong Li, Xutong Niu).

Photogrammetric Engineering & Remote Sensing
Vol. 90, No. 5, May 2024, pp. 313–323.
0099-1112/22/313–323

doi: 10.14358/PERS.23-00078R2

PEER-REVIEWED CONTENT IS ONLY AVAILABLE TO ASPRS MEMBERS AND SUBSCRIBERS

FOR MORE INFORMATION VISIT MY.ASPRS.ORG

PEER-REVIEWED CONTENT
IS ONLY AVAILABLE TO
ASPRS MEMBERS AND SUBSCRIBERS

FOR MORE INFORMATION VISIT
MY.ASPRS.ORG

PEER-REVIEWED CONTENT
IS ONLY AVAILABLE TO
ASPRS MEMBERS AND SUBSCRIBERS

FOR MORE INFORMATION VISIT
MY.ASPRS.ORG

PEER-REVIEWED CONTENT
IS ONLY AVAILABLE TO
ASPRS MEMBERS AND SUBSCRIBERS

FOR MORE INFORMATION VISIT
MY.ASPRS.ORG

PEER-REVIEWED CONTENT
IS ONLY AVAILABLE TO
ASPRS MEMBERS AND SUBSCRIBERS

FOR MORE INFORMATION VISIT
MY.ASPRS.ORG

PEER-REVIEWED CONTENT
IS ONLY AVAILABLE TO
ASPRS MEMBERS AND SUBSCRIBERS

FOR MORE INFORMATION VISIT
MY.ASPRS.ORG

PEER-REVIEWED CONTENT
IS ONLY AVAILABLE TO
ASPRS MEMBERS AND SUBSCRIBERS

FOR MORE INFORMATION VISIT
MY.ASPRS.ORG

PEER-REVIEWED CONTENT
IS ONLY AVAILABLE TO
ASPRS MEMBERS AND SUBSCRIBERS

FOR MORE INFORMATION VISIT
MY.ASPRS.ORG

SUSTAININGMEMBERS

Aerial Services, Inc.
Cedar Falls, Iowa
www.AerialServicesInc.com
Member Since: 5/2001

Airworks Solutions Inc.
Boston, Massachusetts
Member Since: 5/2022

Applanix
Richmond Hill, Ontario, Canada
http://www.applanix.com
Member Since: 7/1997

Ayres Associates
Madison, Wisconsin
www.AyresAssociates.com
Member Since: 1/1953

Dewberry
Fairfax, Virginia
www.dewberry.com
Member Since: 1/1985

Digital Mapping, Inc.(DMI)
Huntington Beach, California
www.admap.com
Member Since: 4/2002

Environmental Research Incorporated
Linden, Virginia
www.eri.us.com
Member Since: 8/2008

Esri
Redlands, California
www.esri.com
Member Since: 1/1987

GeoCue Group
Madison, Alabama
http://www.geocue.com
Member Since: 10/2003

GeoDyn GmbH
Munich, Germany
www.geodyn.com/index
Member Since: 3/2024

Geographic Imperatives LLC
Centennial, Colorado
Member Since: 12/2020

GPI Geospatial Inc.
Orlando, Florida
www.aca-net.com
Member Since: 1/1994

Halff Associates, Inc.
Richardson, Texas
www.halff.com
Member Since: 8/2021

Keystone Aerial Surveys, Inc.
Philadelphia, Pennsylvania
www.kasurveys.com
Member Since: 1/1985

Kucera International
Willoughby, Ohio
www.kucerainternational.com
Member Since: 1/1992

L3Harris Technologies
Broomfield, Colorado
www.l3harris.com
Member Since: 6/2008

Merrick & Company
Greenwood Village, Colorado
www.merrick.com
Member Since: 4/1995

Miller Creek Associates
SeaTac Washington
www.mcamaps.com
Member Since: 12/2014

Nearmap
South Jordan, Utah
www.nearmap.com
Member Since: 6/2023

NV5 Geospatial
Sheboygan Falls, Wisconsin
www.quantumspatial.com
Member Since: 1/1974

Pickett and Associates, Inc.
Bartow, Florida
www.pickettusa.com
Member Since: 4/2007

PixElement
Belmont, Michigan
https://pixelement.com
Member Since: 2/2017

Riegl USA, Inc.
Orlando, Florida
www.rieglusa.com
Member Since: 11/2004

RRC International, LLC
Round Rock, Texas
https://rrccompanies.com/
Member Since: 9/2023

Sanborn Map Company
Colorado Springs, Colorado
www.sanborn.com
Member Since: 10/1984

Surdex Corporation
Chesterfield, Missouri
www.surdex.com
Member Since: 12/2011

Surveying And Mapping, LLC (SAM)
Austin, Texas
www.sam.biz
Member Since: 12/2005

T3 Global Strategies, Inc.
Bridgeville, Pennsylvania
https://t3gs.com/
Member Since: 6/2020

Towill, Inc.
San Francisco, California
www.towill.com
Member Since: 1/1952

Woolpert LLP
Dayton, Ohio
www.woolpert.com
Member Since: 1/1985

SUSTAININGMEMBER**BENEFITS**

Membership

- ✓ Provides a means for dissemination of new information
- ✓ Encourages an exchange of ideas and communication
- ✓ Offers prime exposure for companies

Benefits of an ASPRS Membership

- Complimentary and discounted Employee Membership*
- E-mail blast to full ASPRS membership*
- Professional Certification Application fee discount for any employee
- Member price for ASPRS publications
- Discount on group registration to ASPRS virtual conferences
- Sustaining Member company listing in ASPRS directory/website
- Hot link to company website from Sustaining Member company listing page on ASPRS website
- Press Release Priority Listing in *PE&RS* Industry News
- Priority publishing of Highlight Articles in *PE&RS* plus, 20% discount off cover fee
- Discount on *PE&RS* advertising
- Exhibit discounts at ASPRS sponsored conferences (exception ASPRS/ILMF)
- Free training webinar registrations per year*
- Discount on additional training webinar registrations for employees
- Discount for each new SMC member brought on board (Discount for first year only)